

Emergence of Nodal-Knot Transitions by Disorder

Ming Gong,^{1,*} Peng-Lu Zhao,^{2,†} Qian Niu,^{2,3} and X. C. Xie^{1,4,5}

¹International Center for Quantum Materials, School of Physics, Peking University, Beijing 100871, China

²Department of Physics, University of Science and Technology of China, Hefei, Anhui 230026, China

³CAS Key Laboratory of Strongly-Coupled Quantum Matter Physics,

University of Science and Technology of China, Hefei, Anhui 230026, China

⁴Institute for Nanoelectronic Devices and Quantum Computing, Fudan University, Shanghai 200433, China.

⁵Hefei National Laboratory, Hefei 230088, China

(Dated: September 4, 2024)

Under certain symmetries, degenerate points in three-dimensional metals form one-dimensional nodal lines. These nodal lines sometimes feature knotted structures and have been studied across diverse backgrounds. As one of the most common physical perturbations, disorder effects often trigger novel quantum phase transitions. For nodal-knot phases, whether disorder can drive knot transitions remains an unclear and intriguing problem. Employing renormalization-group calculations, we demonstrate that nodal-knot transitions emerges in the presence of weak disorder. Specifically, both chemical-potential-type and magnetic-type disorders can induce knot transitions, resulting in the emergence of distinct knot topologies. The transition can be quantitatively reflected in the change of topological invariants such as the knot Wilson loop integrals. Our findings open up a new avenue for manipulating the topology of nodal-knot phases through disorder effects.

Introduction.—In the 1860s, Lord Kelvin’s vortex atom theory introduced the concept of knots to physics, which was further developed by Peter Tait [1, 2]. Despite its unfortunate failure, the efforts made by Kelvin and Tait significantly advanced the mathematical studies of knot theory [1, 2]. A century later, developments of topological quantum field theory revitalized knot theory, and lighting the way to fault-tolerant quantum computation [3–7]. As the condensed matter counterpart of topological quantum field theories, topological bands become ideal platforms for studying the emergence of novel phenomena. Specially, the degenerate points of three-dimensional (3D) topological bands can form one-dimensional (1D) nodal lines under the protection of symmetries [8, 9]. These nodal lines provide a fairyland of knots (nodal-knots) [10–17], and have been studied across a wide range of physical systems beyond condensed matter materials [10, 18–23], including ultra-cold atoms [24–28], photonics [29–33], acoustics [34–36], and topological circuits [37–40]. The focus has also been extended from Hermitian physics to non-Hermitian physics [36, 41–47].

Regardless of the systems that realize nodal-knots, a fundamental question is how these knotted structures can be tuned through perturbations. Unlike traditional symmetry-protected topological phases [48–50], the flexibility of the ways that 1D nodal lines are embedded into the 3D Brillouin zone to form knots enables the manipulations of nodal-knot structures. On the other hand, it is well-known that disorder effects can significantly renormalize the dispersions [51, 52]. Consequently, quantum phase transitions can be triggered and novel orders may emerge. Therefore, a fundamental and intriguing question naturally arises: Can nodal-knot phases of matters be manipulated by disorders?

In this Letter, we address this question by asserting

that knot transitions of nodal-knot phases can be triggered by different types of disorder. Employing two-band models that host nodal-knot degeneracies, we study the evolution of nodal-knots with various knot topologies under weak disorders. With the help of renormalization-group (RG) calculations, we find that both chemical-potential-type disorder and magnetic-type disorder can trigger transitions of knot structures. Different types of disorder lead to evolutions of nodal-knots into different knot structures, as sketched in Fig. 1. Mathematically, these knot transitions can be reflected by the knot Wilson loop integrals, which is a knot invariant and its change can be detected through de Haas-van Alphen experiment. Our results uncover the fascinating interplay between knots, topological phases, and disorder effects, and will be beneficial for studies of nodal-knots in disordered systems across diverse backgrounds.

Model for 3D nodal-knots.—To begin with, we construct the Hamiltonian of 3D nodal-knots. A general two-band Hamiltonian reads $H(\mathbf{k}) = f_0(\mathbf{k})\sigma_0 + \sum_{i=x,y,z} f_i(\mathbf{k})\sigma_i$, where σ_i are the Pauli matrices. In the presence of chiral symmetry $\mathcal{S} = \sigma_z$, the Hamiltonian satisfies

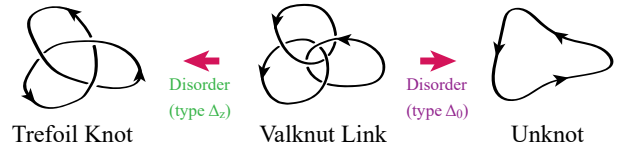


FIG. 1. (color online) Schematics of the knot transition of nodal-knots in the presence of disorder. The nodal line features a valknot linked structure (middle) in the clean limit. Under different types of disorders (highlighted with different colors), it can undergo transitions into a trefoil knot (left) or a single unknot (right).

$SH(\mathbf{k})S^{-1} = -H(\mathbf{k})$, which forces the σ_0 and σ_z terms to vanish. Then

$$H(\mathbf{k}) = f_x(\mathbf{k})\sigma_x + f_y(\mathbf{k})\sigma_y. \quad (1)$$

The models that host different types of nodal-knots can be obtained by setting [11, 12]

$$f_x(\mathbf{k}) = \text{Re}\mathcal{F}_{pq}(\mathbf{k}), \quad f_y(\mathbf{k}) = \text{Im}\mathcal{F}_{pq}(\mathbf{k}) \quad (2)$$

where

$$\begin{aligned} \mathcal{F}_{pq}(\mathbf{k}) = & v_p(k_x + ik_y)^p + v_q[k_z + i(\lambda_1 - \lambda_2 k^2)]^q \\ & + m_1 + im_2. \end{aligned} \quad (3)$$

Here, $k^2 = \sum_{i=x,y,z} k_i^2$, p and q are integers. v_p , v_q , λ_1 , λ_2 , m_1 , and m_2 are parameters that shape the nodal-knot. The degenerate points with $E(\mathbf{k}) = \sqrt{f_x^2(\mathbf{k}) + f_y^2(\mathbf{k})} = 0$ determine the nodal lines in momentum space. When $v_p = v_q \neq 0$, $m_1 = m_2 = 0$, $\lambda_2 = 0.5$, and $\lambda_1 > 0$, the nodal line of $F_{pq}(k)$ form the torus knot (or link) of type (p, q) , thus different choices of (p, q) in $H(\mathbf{k})$ yields different nodal-knots. For example, $(2, 2)$ -the Hopf link, $(2, 3)$ and $(3, 2)$ -the trefoil knot, and $(3, 3)$ -the valknot link (Knot Atlas L6n1). When p and q are relatively prime to each other, the nodal-knot is connected (such as the trefoil knot), otherwise disconnected (such as the Hopf link). The nodal lines of $H(\mathbf{k})$ are oriented, similar to the superconducting or superfluid vortex lines [53]. The orientation is determined by the unit tangent vector [17]

$$\mathbf{T}(\mathbf{k}_0) = \frac{\nabla_{\mathbf{k}} f_x(\mathbf{k}_0) \times \nabla_{\mathbf{k}} f_y(\mathbf{k}_0)}{|\nabla_{\mathbf{k}} f_x(\mathbf{k}_0) \times \nabla_{\mathbf{k}} f_y(\mathbf{k}_0)|}. \quad (4)$$

Here, $\nabla_{\mathbf{k}} = (\partial_{k_x}, \partial_{k_y}, \partial_{k_z})$, and \mathbf{k}_0 represents a regular point, i.e., not the touching point (TP), on the nodal line.

As we will analyze in the following, when different types of disorder are introduced, m_1 and m_2 in Eq. 3 spontaneously emerge due to renormalization of disorders, triggering the emergence of knot transitions [11].

Disorder effect and RG equations.—We model the disorder potential by a coupling term $H_{\text{dis}} = \int d^3\mathbf{r} U_\nu(\mathbf{r}) \psi^\dagger(\mathbf{r}) \sigma_\nu \psi(\mathbf{r})$, where $\nu=0$ denotes the chemical-potential type disorder and $\nu=x, y, z$ denote the magnetic-type disorders in three directions [54]. $U_\nu(\mathbf{r})$ is the disorder potential of a Gaussian white noise with probability distribution $p[U_\nu(\mathbf{r})] \propto \exp[-1/2\Delta_\nu U_\nu^2(\mathbf{r})]$ and spatial correlation $\langle U_\nu(\mathbf{r}) U_\rho(\mathbf{r}') \rangle = \delta_{\nu\rho} \delta(\mathbf{r}-\mathbf{r}')$. Through the replica method [51, 52, 55], the fermionic mode $\psi(\mathbf{r}, \tau)$ is replicated into N copies as $\psi_i(\mathbf{r}, \tau)$ ($i = 1 \cdots N$) (Supplementary Materials, Sec. I [56]). In this way, the ensemble average results in an effective attractive interaction between replica fields with strength Δ_ν . The effective action in Euclidean

spacetime then reads

$$\begin{aligned} S = & \int d^3\mathbf{r} d\tau \mathcal{L}_0 + \int d^3\mathbf{r} d\tau d\tau' \mathcal{L}_{\text{dis}}, \\ \mathcal{L}_0 = & \sum_{i=1}^N \bar{\psi}_i(\mathbf{r}, \tau) [\partial_\tau + H(\mathbf{r}, \nabla_{\mathbf{r}}, \cdots)] \psi_i(\mathbf{r}, \tau), \\ \mathcal{L}_{\text{dis}} = & - \sum_{i,j=1}^N \sum_{\nu=0,x,y,z} \frac{\Delta_\nu}{2} (\bar{\psi}_i \sigma_\nu \psi_i)_{\mathbf{r},\tau} (\bar{\psi}_j \sigma_\nu \psi_j)_{\mathbf{r},\tau'}. \end{aligned} \quad (5)$$

Here, $H(\mathbf{r}, \nabla_{\mathbf{r}}, \cdots)$ is the coordinate space representation of $H(\mathbf{k})$. \mathcal{L}_0 and \mathcal{L}_{dis} are Lagrangians of the free part and disorder part respectively.

We then perform the Wilsonian momentum-shell RG calculations [52, 56–58], and set the momentum cut off as Λ . By integrating the fermionic modes inside the momentum-shell defined by $e^{-dl}\Lambda < |\mathbf{k}| < \Lambda$ and rescaling the momentum as $\mathbf{k} \rightarrow e^{-dl}\mathbf{k}$, we investigate the running of parameters v_p , v_q , λ_1 , λ_2 , m_1 , m_2 , and disorder strengths $\Delta_{0,x,y,z}$ with respect to the running scale l . The RG equations for parameters v_p , v_q , λ_1 , λ_2 , m_1 , and m_2 read (Supplementary Materials, Sec. V [56])

$$\begin{aligned} dv_p/dl = & (1-p)v_p, \quad dv_q/dl = (1-q)v_q, \\ d\lambda_1/dl = & \lambda_1, \quad d\lambda_2/dl = -\lambda_2, \\ dm_1/dl = & m_1 + (-\Delta_0 - \Delta_x + \Delta_y + \Delta_z)\mathcal{G}_1^x, \\ dm_2/dl = & m_2 + (-\Delta_0 + \Delta_x - \Delta_y + \Delta_z)\mathcal{G}_1^y. \end{aligned} \quad (6)$$

Here, $\mathcal{G}_1^{(x/y)} = -\frac{1}{2dl} \int_{\text{shell}} \frac{d^3\mathbf{k}}{(2\pi)^3} \text{Tr}[\sigma_{x/y} G(\mathbf{k}, \omega=0)]$, with $G(\mathbf{k}, \omega) = [i\omega - H(\mathbf{k})]^{-1}$ being the Green's function and $H(\mathbf{k})$ given by Eq. (1). The integral is performed on the momentum-shell as $e^{-dl}\Lambda < |\mathbf{k}| < \Lambda$.

In the following, we consider one type of disorder at a time. We take the chemical-potential-type disorder Δ_0 and the magnetic-type disorder Δ_z for examples. The RG equations for Δ_0 and for Δ_z are

$$d\Delta_0/dl = -\Delta_0 + 2\Delta_0^2(\mathcal{G}_2^{xx} + \mathcal{G}_2^{yy}), \quad (7)$$

$$d\Delta_z/dl = -\Delta_z - 2\Delta_z^2(\mathcal{G}_2^{xx} + \mathcal{G}_2^{yy}). \quad (8)$$

Here, $\mathcal{G}_2^{(xx/yy)} = \frac{1}{4dl} \int_{\text{shell}} \frac{d^3\mathbf{k}}{(2\pi)^3} \text{Tr}[\sigma_{x/y} G(\mathbf{k}, \omega=0)]^2$. The full RG equations can be found in Supplementary Materials [56].

From Eqs. (6), we see that except for rescaling, parameters v_p , v_q , λ_1 , and λ_2 are not modified by the disorder. In fact, the rescaling of these parameters play no role in the knot transitions since they only affect the relative size of the nodal-knot. In contrast, as shown in Eqs. (6), m_1 and m_2 are renormalized significantly by disorders. Importantly, even under the initial conditions $m_1(l=0)=0$ and $m_2(l=0)=0$, they can emerge at a rate of $\mathcal{O}(\Delta)$. This result suggests that under the renormalization of disorder, m_1 and m_2 are far from fixed points, being the relevant parameters that trigger the transitions.

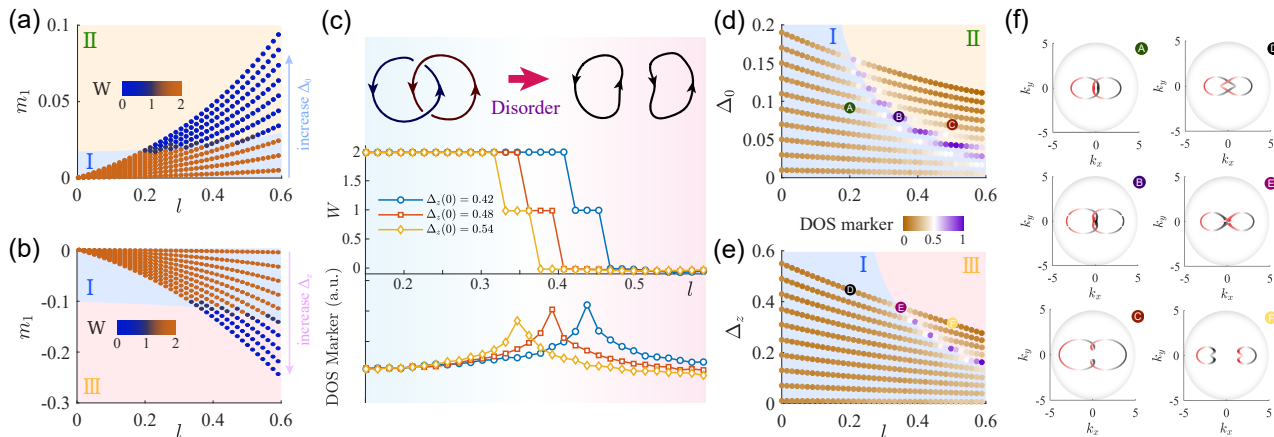


FIG. 2. (color online) Renormalization-group (RG) flows of Hopf linked nodal-knots. (a) and (b), the RG flows of m_1 under the renormalization of Δ_0 and Δ_z , respectively. The flow curves are colored by the knot Wilson loop W , and colored regions denote I the Hopf link, II the unknot, and III the unlink. (c), the RG flows of the knot Wilson loop (upper panel) and the density of states (DOS) marker (lower panel) under the renormalization of Δ_z with different initial values. (d) and (e), the RG flows of Δ_0 and Δ_z , respectively. The flow curves are colored by the DOS marker. The colored regions I, II, and III are the same as that in (a) and (b). The corresponding nodal-knot configurations of representative points labeled A-F on the RG curves are plotted in (f), colored by the y -component of unit tangent vector $T_y(\mathbf{k})$ [defined in Eq. (4)].

We analyse the renormalization of the parameters through numerically solving the RG equations Eqs.(6,7,8). As an example, we take $p=q=2$, and set the initial conditions at $l=0$ as $v_p(0)=v_q(0)=0.1$, $m_1(0)=m_2(0)=0$, $\lambda_1(0)=0.4$, and $\lambda_2(0)=0.5$. This set of parameters describe the hopf linked nodal-knot in the clean limit (corresponding to the nodal-knot configuration in the absence of the disorder effect). The momentum cut off takes $\Lambda=5$. We show the results of the RG flow of m_1 in Fig.2 (a) and (b) under different initial disorder strength $\Delta_0(l=0)$ or $\Delta_z(l=0)$, together with the RG flows of Δ_0 and Δ_z in Fig.2 (d) and (e) [59]. Here, m_2 keeps zero for that the momentum-shell integration forces \mathcal{G}_1^y to vanish [56]. Clearly, both Δ_0 and Δ_z can drive the emergence of m_1 , but in opposite signs. Similar results also hold for $p=q=3$, the valknot link [Fig.3 (a) and (b)]. This strongly implies that different types of disorders can trigger different knot transitions. However, only the RG flow of these parameters is not adequate for displaying the features and types of the knot transitions, a more intuitional mathematical object, e.g., a topological invariant, is needed.

Knot invariants and knot transitions in (2,2) and (3,3) systems.—Unlike band topological numbers such as TKNN numbers [60] and Z_2 numbers [48–50] that unambiguously characterize the symmetry-protected topological phases, the complexity of knots makes it mathematically impossible to find a knot invariant that can provide a one-to-one characterization of the knot configuration. Nevertheless, knot invariants, of which the jumps can adequately reveal nodal-knot transitions, can still be calculated. Here, we adopt the knot Wilson loop integral W in conjunction with the DOS marker to determine

the nodal-knot transitions [5, 14]. The knot Wilson loop integral is

$$W(L_1, \dots, L_N) = \frac{1}{\pi} \oint_{l \in L_1, \dots, L_N} \mathbf{A}(\mathbf{k}) \cdot d\mathbf{l}. \quad (9)$$

Here, L_1, \dots, L_N denote N oriented nodal loops, and the orientation of the integral path l is determined by the tangent vector $\mathbf{T}(\mathbf{k}_0)$ in Eq. (4). $\mathbf{A}(\mathbf{k}) = -i\langle u_{\mathbf{k}} | \partial_{\mathbf{k}} | u_{\mathbf{k}} \rangle$ is the Berry connection. It should be noted that $\mathbf{A}(\mathbf{k})$ on the degenerate nodal lines are not well-defined, the integral path should be slightly deviate from the nodal lines, and this procedure is called to “frame” the knots into strands [5, 14]. Mathematically, $W(L_1, \dots, L_N)$ is the sum of the linking numbers Ψ_{ij} of loops L_i and L_j if $i \neq j$, and Ψ_{ii} would be the Gauss linking number of the loop L_i and its frame [1, 2, 61]. Physically, the knot Wilson loop integral W reflects the Berry phase accumulated by electrons as they move along the intertwined nodal lines. For the Hopf-linked nodal-knot, each of the electrons moving along the nodal loops L_1 and L_2 gain π Berry phase, thus $W=2$. For the valknot link, each nodal loop interlocks with the other two, and each gains 2π Berry phase, leading to $W=6$ in total.

With this mathematical tool in hand, we can view the nodal-knot transitions more intuitively. We color the RG flows in FIG.2 (a) and (b) with the calculated knot Wilson loop integral W . Moreover, to demonstrate the phase boundaries of nodal-knot transitions more comprehensively, we have supplemented the calculation with the density of states (DOS) marker [colored in the RG flow curves of Δ_0 and Δ_z in FIG.2 (d) and (e)], which counts the number of states within the energy window $[0, \epsilon]$ with ϵ an extremely small energy scale. At the transition

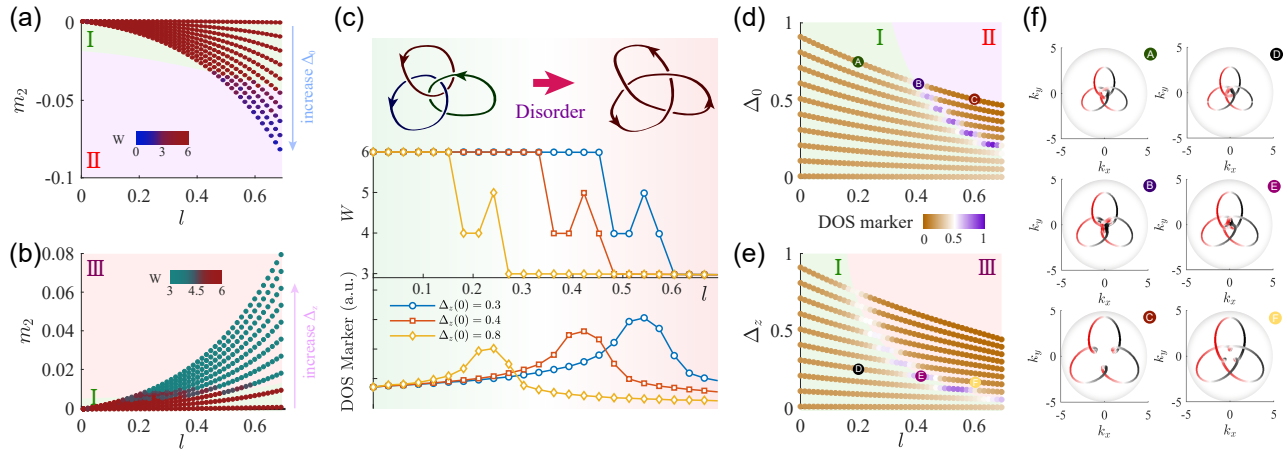


FIG. 3. (color online) Renormalization-group (RG) flows of valknut linked nodal-knots. (a) and (b), the RG flows of m_2 under the renormalization of Δ_0 and Δ_z , respectively. The flow curves are colored by the knot Wilson loop W , and colored regions denote I the valknut link, II the unknot, and III the trefoil knot. (c), the RG flows of the knot Wilson loop (upper panel) and the density of states (DOS) marker (lower panel) under the renormalization of Δ_z with different initial values. (d) and (e), the RG flows of Δ_0 and Δ_z , respectively. The flow curves are colored by the DOS marker. The colored regions I, II, and III are the same as that in (a) and (b). The corresponding nodal-knot configurations of representative points labeled A-F on the RG curves are plotted in (f), colored by the y -component of unit tangent vector $T_y(\mathbf{k})$.

points, the nodal lines should touch and then separate and reconnected, leading to the divergence of the DOS markers. In this way, the transition boundaries can be determined jointly by W and the DOS markers. Specifically, we take three curves in FIG. 2 (b) and plot them in terms of W and the DOS marker in FIG. 2 (c). It is clear that the knot Wilson loop integral W drops from 2 to 0, and for each curve, the DOS markers show clear peaks at the transition points.

To visualize the renormalized nodal-knot configurations, we select six points on the RG flow curves marked A-F in FIG. 2 (d) and (e). The corresponding knot configurations are displayed in FIG. 2 (f). Interestingly, although both Δ_0 and Δ_z drive the transition of W from 2 to 0, the results of these transitions are different. As shown in figure FIG. 2 (f), Δ_0 drives the transition from a Hopf link (A or D) to an unknot (C), while Δ_z drives the transition to an unlink (F). This difference stems from their renormalization effect to the parameters m_1 and m_2 with opposite sign. Therefore, we can divide the RG flow diagrams into regions I (Hopf link), II (unknot), and III (unlink) [shown in FIG. 2 (a,b) and (d,e)].

Similar to the Hopf link, the valknut nodal-knot with $p=q=3$ also experience different transitions under different types of disorder. In parallel to the Hopf link, we show the results of RG flow and the corresponding W and DOS markers [Fig. 3 (a)-(e)]. Here, different from the Hopf link, m_1 keeps zeros and only m_2 got renormalized. We see that under the renormalization of Δ_0 , W jumps from 6 to 0, while under Δ_z , W jumps from 6 to 3, which is distinct from the Hopf links. Moreover, representative nodal-knot configurations shown in Fig. 3

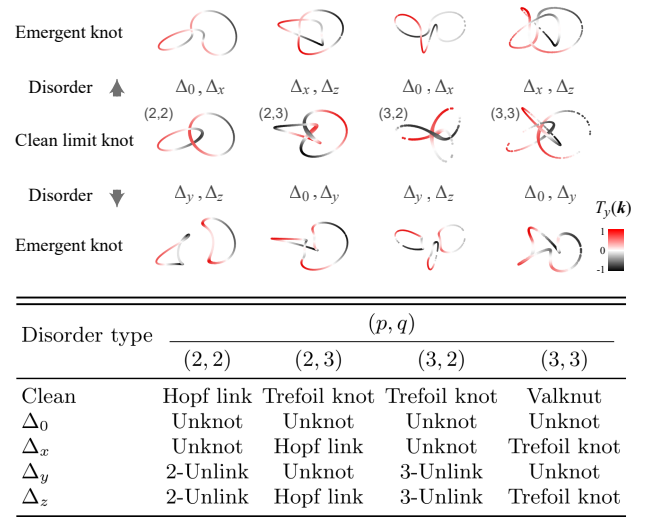


FIG. 4. (color online) Emergent knot configurations under different types of disorders. The middle line of the figure shows the clean limit nodal-knots, with various (p, q) . Specifically, (2, 2)-the Hopf link, (2, 3) and (3, 2)-the trefoil knot, and (3, 3)-the valknut. The y -component of unit tangent vector $T_y(\mathbf{k})$ is colored on the nodal-knots. The table below summarize the disorder driven nodal-knot transitions.

(f) suggests that we can similarly divide the RG flow into regions I, II, and III, which describe the nodal-knot configurations of valknut, unknot, and trefoil knot, respectively. Note that under Δ_z , the originally linked valknut evolve into the trefoil knot, which is a knotted structure, in sharp contrast to the case of the Hopf link which evolve into either unknot or unlink.

As summarized in Fig. 4, we can conclude that the ability of different types of disorder to induce different types of nodal-knot transitions is universal. Especially, the presence of magnetic disorders can diversify the knot configurations (see the table in Fig. 4), giving rise to the emergence of non-trivial nodal-knots from their clean limit. This finding plays a crucial role in realizing and manipulating topological knotted phases in various systems in the future.

Discussions.—Nodal line semimetals with non-trivial knotted or linked structures have been confirmed to exist in solid materials, such as Co_2MnGa through ARPES experiments [10, 23]. In the presence of disorder, the ARPES observations would be affected by the renormalization of the low-energy band structure. Our work predicts the possibility of disorder induced nodal-knot transitions under doping with magnetic or non-magnetic disorders, which awaits further experimental verification. Furthermore, the knot Wilson loop integral W provides the total Berry phase accumulated by the non-trivial knotted structure. Nodal-knot transitions would result in changes of Berry phase, inducing the phase shift in quantum oscillations [62, 63]. Therefore, the nodal-knot transitions can also be tested through de Haas-van Alphen experiments [56, 64–66] by observing the π phase shifts in the quantum oscillations of the transport observables.

Aside from the solid materials, it is also achievable to introduce and control disorders in artificial systems such as cold atoms or acoustic and optical systems [25, 32, 36]. Especially, introducing noise in cold atoms, or utilizing the optical speckle field can simulate the disorder effect [67]. Moreover, optical Raman lattice can simulate the spin-orbital coupling together with the long-range hopping [68], which can achieve the magnetic disorder potentials [28]. In these ways, magnetization directions of the disorders can be controlled easier. Therefore, our work provides theoretical supports for future studies of knotted topological phases and disorder-induced knot transitions in these systems.

We acknowledge helpful discussions with Xing-Can Yao, Qing-Feng Sun, Hua Jiang, Chui-Zhen Chen, and Xinchu Zhou. This work is supported by the National Natural Science Foundation of China (Grants No. 12304074, No. 12047531, and No. 12234017), and the Innovation Program for Quantum Science and Technology (No. 2021ZD0302400), Ming Gong is also supported by China National Postdoctoral Program for Innovative Talents (Grants No. BX20240004).

* minggong@pku.edu.cn

† zhaoplu@gmail.com

[1] J. C. Baez and J. P. Muniain, *Gauge Fields, Knots and Gravity* (World Scientific Publishing Company, Singapore ; River Edge, N.J, 1994).

- [2] S. H. Simon, *Topological Quantum* (Oxford University Press, Oxford, New York, 2023).
- [3] M. F. Atiyah, Topological Quantum Field Theory, *Publ. Math-Paris* **68**, 175 (1988).
- [4] E. Witten, Topological Quantum Field Theory, *Commun. Math. Phys.* **117**, 353 (1988).
- [5] E. Witten, Quantum field theory and the Jones polynomial, *Commun. Math. Phys.* **121**, 351 (1989).
- [6] C. Blanchet, N. Habegger, G. Masbaum, and P. Vogel, Topological Quantum Field Theories Derived from the Kauffman Bracket, *Topology* **34**, 883 (1995).
- [7] C. Nayak, S. H. Simon, A. Stern, M. Freedman, and S. Das Sarma, Non-Abelian Anyons and Topological Quantum Computation, *Rev. Mod. Phys.* **80**, 1083 (2008).
- [8] A. A. Burkov, M. D. Hook, and L. Balents, Topological Nodal Semimetals, *Phys. Rev. B* **84**, 235126 (2011).
- [9] C. Fang, H. Weng, X. Dai, and Z. Fang, Topological Nodal Line Semimetals, *Chin. Phys. B* **25**, 117106 (2016).
- [10] G. Chang, S.-Y. Xu, X. Zhou, S.-M. Huang, B. Singh, B. Wang, I. Belopolski, J. Yin, S. Zhang, A. Bansil, H. Lin, and M. Z. Hasan, Topological Hopf and Chain Link Semimetal States and Their Application to Co_2MnGa , *Phys. Rev. Lett.* **119**, 156401 (2017).
- [11] R. Bi, Z. Yan, L. Lu, and Z. Wang, Nodal-Knot Semimetals, *Phys. Rev. B* **96**, 201305(R) (2017).
- [12] M. Ezawa, Topological Semimetals Carrying Arbitrary Hopf Numbers: Fermi Surface Topologies of a Hopf Link, Solomon's Knot, Trefoil Knot, and other Linked Nodal Varieties, *Phys. Rev. B* **96**, 041202(R) (2017).
- [13] Z. Yan, R. Bi, H. Shen, L. Lu, S.-C. Zhang, and Z. Wang, Nodal-Link Semimetals, *Phys. Rev. B* **96**, 041103(R) (2017).
- [14] B. Lian, C. Vafa, F. Vafa, and S.-C. Zhang, Chern-Simons theory and Wilson loops in the Brillouin zone, *Phys. Rev. B* **95**, 094512 (2017).
- [15] J. Ahn, D. Kim, Y. Kim, and B.-J. Yang, Band Topology and Linking Structure of Nodal Line Semimetals with \mathbb{Z}_2 Monopole Charges, *Phys. Rev. Lett.* **121**, 106403 (2018).
- [16] Q. Wu, A. A. Soluyanov, and T. Bzdusek, Non-Abelian Band Topology in Noninteracting Metals, *Science* **365**, 1273 (2019).
- [17] Z. Yang, C.-K. Chiu, C. Fang, and J. Hu, Jones Polynomial and Knot Transitions in Hermitian and Non-Hermitian Topological Semimetals, *Phys. Rev. Lett.* **124**, 186402 (2020).
- [18] T. Bzdusek, Q. Wu, A. Rüegg, M. Sigrist, and A. A. Soluyanov, Nodal-Chain Metals, *Nature* **538**, 75 (2016).
- [19] X.-Q. Sun, B. Lian, and S.-C. Zhang, Double Helix Nodal Line Superconductor, *Phys. Rev. Lett.* **119**, 147001 (2017).
- [20] C. Li, C.-M. Wang, B. Wan, X. Wan, H.-Z. Lu, and X.-C. Xie, Rules for Phase Shifts of Quantum Oscillations in Topological Nodal-Line Semimetals, *Phys. Rev. Lett.* **120**, 146602 (2018).
- [21] C. H. Lee, H. H. Yap, T. Tai, G. Xu, X. Zhang, and J. Gong, Enhanced Higher Harmonic Generation from Nodal Topology, *Phys. Rev. B* **102**, 035138 (2020).
- [22] T. Tai and C. H. Lee, Anisotropic Nonlinear Optical Response of Nodal-loop Materials, *Phys. Rev. B* **103**, 195125 (2021).
- [23] I. Belopolski, G. Chang, T. A. Cochran, Z.-J. Cheng, X. P. Yang, C. Hugelmeier, K. Manna, J.-X. Yin, G. Cheng, D. Multer, M. Litskevich, N. Shumiya, S. S.

- Zhang, C. Shekhar, N. B. M. Schröter, A. Chikina, C. Polley, B. Thiagarajan, M. Leandersson, J. Adell, S.-M. Huang, N. Yao, V. N. Strocov, C. Felser, and M. Z. Hasan, Observation of a Linked-loop Quantum State in a Topological Magnet, *Nature* **604**, 647 (2022).
- [24] C. Wang, P. Zhang, X. Chen, J. Yu, and H. Zhai, Scheme to Measure the Topological Number of a Chern Insulator from Quench Dynamics, *Phys. Rev. Lett.* **118**, 185701 (2017).
- [25] D.-L. Deng, S.-T. Wang, K. Sun, and L.-M. Duan, Probe Knots and Hopf Insulators with Ultracold Atoms, *Chin. Phys. Lett.* **35**, 013701 (2018).
- [26] M. Tarnowski, F. N. Únal, N. Fläschner, B. S. Rem, A. Eckardt, K. Sengstock, and C. Weitenberg, Measuring Topology From Dynamics by Obtaining the Chern Number from a Linking Number, *Nat. Commun.* **10**, 1728 (2019).
- [27] F. N. Únal, A. Eckardt, and R.-J. Slager, Hopf Characterization of Two-dimensional Floquet Topological Insulators, *Phys. Rev. Res.* **1**, 022003(R) (2019).
- [28] B. Song, C. He, S. Niu, L. Zhang, Z. Ren, X.-J. Liu, and G.-B. Jo, Observation of Nodal-line Semimetal with Ultracold Fermions in an Optical Lattice, *Nat. Phys.* **15**, 911 (2019).
- [29] J. Leach, M. R. Dennis, J. Courtial, and M. J. Padgett, Knotted Threads of Darkness, *Nature* **432**, 165 (2004).
- [30] W. T. M. Irvine and D. Bouwmeester, Linked and Knotted Beams of Light, *Nat. Phys.* **4**, 716 (2008).
- [31] H. Kedia, I. Bialynicki-Birula, D. Peralta-Salas, and W. T. M. Irvine, Tying Knots in Light Fields, *Phys. Rev. Lett.* **111**, 150404 (2013).
- [32] E. Yang, B. Yang, O. You, H.-C. Chan, P. Mao, Q. Guo, S. Ma, L. Xia, D. Fan, Y. Xiang, and S. Zhang, Observation of Non-Abelian Nodal Links in Photonics, *Phys. Rev. Lett.* **125**, 033901 (2020).
- [33] M. Jayaseelan, J. D. Murphree, J. T. Schultz, J. Ruostekoski, and N. P. Bigelow, Topological Atom Optics and Beyond with Knotted Quantum Wavefunctions, *Commun. Phys.* **7**, 1 (2024).
- [34] Q. Yan, R. Liu, Z. Yan, B. Liu, H. Chen, Z. Wang, and L. Lu, Experimental Discovery of Nodal Chains, *Nat. Phys.* **14**, 461 (2018).
- [35] H. Qiu, Q. Zhang, T. Liu, X. Fan, F. Zhang, and C. Qiu, Minimal Non-Abelian Nodal Braiding in Ideal Metamaterials, *Nat. Commun.* **14**, 1261 (2023).
- [36] Q. Zhang, Y. Li, H. Sun, X. Liu, L. Zhao, X. Feng, X. Fan, and C. Qiu, Observation of Acoustic Non-Hermitian Bloch Braids and Associated Topological Phase Transitions, *Phys. Rev. Lett.* **130**, 017201 (2023).
- [37] L. Li, C. H. Lee, and J. Gong, Emergence and Full 3D-imaging of Nodal Boundary Seifert Surfaces in 4D Topological Matter, *Commun. Phys.* **2**, 1 (2019).
- [38] C. H. Lee, A. Sutrisno, T. Hofmann, T. Helbig, Y. Liu, Y. S. Ang, L. K. Ang, X. Zhang, M. Greiter, and R. Thomale, Imaging Nodal Knots in Momentum Space Through Topoelectrical Circuits, *Nat. Commun.* **11**, 4385 (2020).
- [39] X. Zhang, G. Li, Y. Liu, T. Tai, R. Thomale, and C. H. Lee, Tidal Surface States as Fingerprints of non-Hermitian Nodal Knot Metals, *Commun. Phys.* **4**, 1 (2021).
- [40] Z. Wang, X.-T. Zeng, Y. Biao, Z. Yan, and R. Yu, Realization of a Hopf Insulator in Circuit Systems, *Phys. Rev. Lett.* **130**, 057201 (2023).
- [41] J. Carlström, M. Stålhammar, J. C. Budich, and E. J. Bergholtz, Knotted Non-Hermitian Metals, *Phys. Rev. B* **99**, 161115(R) (2019).
- [42] Z. Yang and J. Hu, Non-Hermitian Hopf-Link Exceptional Line Semimetals, *Phys. Rev. B* **99**, 081102(R) (2019).
- [43] H. Hu and E. Zhao, Knots and Non-Hermitian Bloch Bands, *Phys. Rev. Lett.* **126**, 010401 (2021).
- [44] E. J. Bergholtz, J. C. Budich, and F. K. Kunst, Exceptional Topology of Non-Hermitian Systems, *Rev. Mod. Phys.* **93**, 015005 (2021).
- [45] Y. S. S. Patil, J. Höller, P. A. Henry, C. Guria, Y. Zhang, L. Jiang, N. Kralj, N. Read, and J. G. E. Harris, Measuring the Knot of Non-Hermitian Degeneracies and Non-Commuting Braids, *Nature* **607**, 271 (2022).
- [46] C.-X. Guo, S. Chen, K. Ding, and H. Hu, Exceptional Non-Abelian Topology in Multiband Non-Hermitian Systems, *Phys. Rev. Lett.* **130**, 157201 (2023).
- [47] J. Chen, Z. Wang, Y.-T. Tan, C. Wang, and J. Ren, Machine Learning of Knot Topology in Non-Hermitian Band Braids, [arxiv.2401.10908](https://arxiv.org/abs/2401.10908) (2024).
- [48] C. L. Kane and E. J. Mele, Quantum Spin Hall Effect in Graphene, *Phys. Rev. Lett.* **95**, 226801 (2005).
- [49] L. Fu, C. L. Kane, and E. J. Mele, Topological Insulators in Three Dimensions, *Phys. Rev. Lett.* **98**, 106803 (2007).
- [50] L. Fu and C. L. Kane, Topological Insulators with Inversion Symmetry, *Phys. Rev. B* **76**, 045302 (2007).
- [51] P. A. Lee and T. V. Ramakrishnan, Disordered Electronic Systems, *Rev. Mod. Phys.* **57**, 287 (1985).
- [52] A. Altland and B. D. Simons, *Condensed Matter Field Theory*, 2nd ed. (Cambridge University Press, Cambridge, 2010).
- [53] G. E. Volovik, *The Universe in a Helium Droplet*, 1st ed. (Clarendon Press, Oxford : New York, 2003).
- [54] A. W. W. Ludwig, M. P. A. Fisher, R. Shankar, and G. Grinstein, Integer Quantum Hall Transition: An Alternative Approach and Exact Results, *Phys. Rev. B* **50**, 7526 (1994).
- [55] F. Wegner, The Mobility Edge Problem: Continuous Symmetry and a Conjecture, *Z. Phys. B: Condens. Matter* **35**, 207 (1979).
- [56] See Supplementary Materials, which includes Refs. [69–73].
- [57] J. Cardy, *Scaling and Renormalization in Statistical Physics*, Cambridge Lecture Notes in Physics (Cambridge University Press, Cambridge, 1996).
- [58] M. Kardar, *Statistical Physics of Fields* (Cambridge University Press, Cambridge, 2007).
- [59] From Eqs. (7) and (8), we see that Δ_0 and Δ_z flow toward zero when they are small. However, we should emphasize that only Δ_z can be viewed as irrelevant parameter because $d\Delta_z/dl$ is always negative. For Δ_0 , as the RG operation proceeds, it will increase again and flow to infinity due to the increase in \mathcal{G}_2^{xx} and \mathcal{G}_2^{yy} in Eq. (7). Therefore, Δ_0 will eventually drive the system to a Diffusive Metal phase after the knot transitions. The result is consistent with the numerical study [74].
- [60] D. J. Thouless, M. Kohmoto, M. P. Nightingale, and M. den Nijs, Quantized Hall Conductance in a Two-Dimensional Periodic Potential, *Phys. Rev. Lett.* **49**, 405 (1982).
- [61] To faithfully reflect the knot topology, a proper frame should be chosen such that an unknotted loop has no

- contribution to *W*.
- [62] G. P. Mikitik and Y. V. Sharlai, Manifestation of Berry's Phase in Metal Physics, *Phys. Rev. Lett.* **82**, 2147 (1999).
- [63] D. Xiao, M.-C. Chang, and Q. Niu, Berry phase effects on electronic properties, *Rev. Mod. Phys.* **82**, 1959 (2010).
- [64] J. Hu, Z. Tang, J. Liu, X. Liu, Y. Zhu, D. Graf, K. Myhro, S. Tran, C. N. Lau, J. Wei, and Z. Mao, Evidence of Topological Nodal-Line Fermions in ZrSiSe and ZrSiTe, *Phys. Rev. Lett.* **117**, 016602 (2016).
- [65] M. N. Ali, L. M. Schoop, C. Garg, J. M. Lippmann, E. Lara, B. Lotsch, and S. S. P. Parkin, Butterfly magnetoresistance, quasi-2D Dirac Fermi surface and topological phase transition in ZrSiS, *Science Advances* **2**, e1601742 (2016).
- [66] S. Pezzini, M. R. van Delft, L. M. Schoop, B. V. Lotsch, A. Carrington, M. I. Katsnelson, N. E. Hussey, and S. Wiedmann, Unconventional mass enhancement around the Dirac nodal loop in ZrSiS, *Nat. Phys.* **14**, 178 (2018).
- [67] S. S. Kondov, W. R. McGehee, J. J. Zirbel, and B. DeMarco, Three-Dimensional Anderson Localization of Ultracold Matter, *Science* [10.1126/science.1209019](https://doi.org/10.1126/science.1209019) (2011).
- [68] H. Miyake, G. A. Siviloglou, C. J. Kennedy, W. C. Burton, and W. Ketterle, Realizing the Harper Hamiltonian with Laser-Assisted Tunneling in Optical Lattices, *Phys. Rev. Lett.* **111**, 185302 (2013).
- [69] P.-L. Zhao, X.-B. Qiang, H.-Z. Lu, and X.-C. Xie, Coulomb Instabilities of a Three-Dimensional Higher-Order Topological Insulator, *Phys. Rev. Lett.* **127**, 176601 (2021).
- [70] P.-L. Zhao, H.-Z. Lu, and X.-C. Xie, Theory for Magnetic-Field-Driven 3D Metal-Insulator Transitions in the Quantum Limit, *Phys. Rev. Lett.* **127**, 046602 (2021).
- [71] H. Isobe and L. Fu, Supermetal, *Phys. Rev. Res.* **1**, 033206 (2019).
- [72] X. Luo, B. Xu, T. Ohtsuki, and R. Shindou, Quantum Multicriticality in Disordered Weyl Semimetals, *Phys. Rev. B* **97**, 045129 (2018).
- [73] P. Goswami and S. Chakravarty, Quantum Criticality Between Topological and Band Insulators in $3 + 1$ Dimensions, *Phys. Rev. Lett.* **107**, 196803 (2011).
- [74] K.-X. Jia, X.-Y. Liu, R. Ma, H. Geng, L. Sheng, and D.-Y. Xing, Phase Diagram of Three Dimensional Disordered Nodal-line Semimetals: Weak Localization to Anderson Localization, *New J. Phys.* **25**, 113033 (2023).

Supplementary Materials for “Emergence of Nodal-Knot Transitions by Disorder”

Ming Gong,^{1,*} Peng-Lu Zhao,^{2,†} Qian Niu,^{2,3} and X. C. Xie^{1,4,5}

¹*International Center for Quantum Materials, School of Physics, Peking University, Beijing 100871, China*

²*Department of Physics, University of Science and Technology of China, Hefei, Anhui 230026, China*

³*CAS Key Laboratory of Strongly-Coupled Quantum Matter Physics,*

University of Science and Technology of China, Hefei, Anhui 230026, China

⁴*Institute for Nanoelectronic Devices and Quantum Computing, Fudan University, Shanghai 200433, China.*

⁵*Hefei National Laboratory, Hefei 230088, China*

CONTENTS

I. Fermionic system under quenched disordered: the replica treatment	S1
II. Fourier transformations	S2
III. RG step 1: coarse grain	S3
IV. RG step 2: rescale	S8
V. RG step 3: renormalization and the RG equations	S9
VI. Knot Wilson loop integrals	S10
VII. Discussions on de Haas-van Alphen experiments	S13
References	S14

I. FERMIONIC SYSTEM UNDER QUENCHED DISORDERED: THE REPLICA TREATMENT

In the presence of a quenched disorder potential $A_m V_m(\mathbf{r})$ (here, A_m may be some matrix to represent different types of disorder), the partition function for a non-interacting fermion system reads [1–3]:

$$\mathcal{Z} = \int \mathcal{D}[\psi, \bar{\psi}] e^{-S_0 - S_{\text{dis}}} \quad (\text{S1})$$

where the free part of the action is:

$$S_0 = - \int d^3\mathbf{r} d^3\mathbf{r}' d\tau d\tau' \bar{\psi}(\mathbf{r}, \tau) \mathbf{G}_0^{-1}(\mathbf{r}, \tau, \mathbf{r}', \tau') \psi(\mathbf{r}', \tau') \quad (\text{S2})$$

with \mathbf{G}_0 the Green’s function of free fermions, and $\tau = it$. The disorder part:

$$S_{\text{dis}} = \int d^3\mathbf{r} d\tau \bar{\psi}(\mathbf{r}, \tau) \left[\sum_{m=1}^M A_m V_m(\mathbf{r}) \right] \psi(\mathbf{r}, \tau). \quad (\text{S3})$$

The total free energy of the system is the disorder averaged logarithmic partition function:

$$\begin{aligned} \mathcal{W} &= -\langle \ln \mathcal{Z} \rangle_{\text{dis}} \\ &= \int \mathcal{D}[V_1] \cdots \mathcal{D}[V_M] P[V_1] \cdots P[V_M] \ln \mathcal{Z} \end{aligned} \quad (\text{S4})$$

* minggong@pku.edu.cn

† zhaoplu@gmail.com

with M types of disorders, and $P[V_m]$ is the distribution functional of the disorder potential. Here we consider that the disorders have no spatial correlations, i.e., $\langle V_m(\mathbf{r})V_n(\mathbf{r}') \rangle = \delta_{mn}\delta(\mathbf{r} - \mathbf{r}')$, and fluctuates with a Gaussian white noise distribution. $P[V_m]$ is assumed to have the form:

$$p[V_m] \propto e^{-\frac{1}{2\Delta_m}V_m^2}. \quad (\text{S5})$$

Here Δ_m represents the fluctuation ‘‘width’’ of the disorder potential $A_m V_m(\mathbf{r})$, which can be understood as the disorder strength. Using the replica method:

$$\langle \ln \mathcal{Z} \rangle_{\text{dis}} = \lim_{N \rightarrow 0} \left\langle \frac{\mathcal{Z}^N - 1}{N} \right\rangle_{\text{dis}}, \quad (\text{S6})$$

the original system is replaced by N identical copies that share the same disorder potential. Here we first evaluate \mathcal{Z}^N

$$\langle \mathcal{Z}^N \rangle_{\text{dis}} = \int \mathcal{D}[V] P[V] \mathcal{D}[\bar{\psi}_1, \psi_1; \dots; \bar{\psi}_N, \psi_N] e^{\int \bar{\psi}_1 \mathbf{G}_0^{-1} \psi_1 + \bar{\psi}_2 \mathbf{G}_0^{-1} \psi_2 + \dots + \bar{\psi}_N \mathbf{G}_0^{-1} \psi_N - \sum_{m=1}^M (\bar{\psi}_1 A_m \psi_1 + \dots + \bar{\psi}_N A_m \psi_N) V_m}. \quad (\text{S7})$$

After averaging over the disorder potentials, the effective partition function becomes:

$$\langle \mathcal{Z}^N \rangle_{\text{dis}} = \int \mathcal{D}[\bar{\psi}_1, \psi_1; \dots; \bar{\psi}_N, \psi_N] e^{\int \bar{\psi}_1 \mathbf{G}_0^{-1} \psi_1 + \bar{\psi}_2 \mathbf{G}_0^{-1} \psi_2 + \dots + \bar{\psi}_N \mathbf{G}_0^{-1} \psi_N + \sum_{i,j=1}^N \sum_{m=1}^M \frac{\Delta_m}{2} \bar{\psi}_i A_m \psi_i \bar{\psi}_j A_m \psi_j}. \quad (\text{S8})$$

At this stage, the effective action of the replicated system is:

$$\begin{aligned} S_{\text{eff}} = & - \int d^3 \mathbf{r} d^3 \mathbf{r}' d\tau d\tau' \sum_{i=1}^N \bar{\psi}_i(\mathbf{r}, \tau) \mathbf{G}_0^{-1}(\mathbf{r}, \tau, \mathbf{r}', \tau') \psi_i(\mathbf{r}', \tau') \\ & - \int d^3 \mathbf{r} d\tau d\tau' \sum_{i,j=1}^N \sum_{m=1}^M \frac{\Delta_m}{2} (\bar{\psi}_i A_m \psi_i)_{\mathbf{r}, \tau} (\bar{\psi}_j A_m \psi_j)_{\mathbf{r}, \tau'}. \end{aligned} \quad (\text{S9})$$

The average over the disorder potential leads to an effective attractive interaction among the replicated fields. At the end of the calculation, the limit $N \rightarrow 0$ should be taken.

II. FOURIER TRANSFORMATIONS

Fourier transforms of field operators in real time:

$$\begin{aligned} \psi(\mathbf{k}, \omega) &= \int d^3 \mathbf{r} dt e^{-i\mathbf{k} \cdot \mathbf{r} + i\omega t} \psi(\mathbf{r}, t) \\ \psi(\mathbf{r}, t) &= \int \frac{d^3 \mathbf{k} d\omega}{(2\pi)^4} e^{i\mathbf{k} \cdot \mathbf{r} - i\omega t} \psi(\mathbf{k}, \omega) \end{aligned} \quad (\text{S10})$$

Fourier transforms of field operators in imaginary time ($t \rightarrow -i\tau$, $\omega_n = \frac{(2n+1)\pi}{\beta}$ is the Matsubara frequency):

$$\begin{aligned} \psi(\mathbf{k}, \omega_n) &= \int_V \int_0^\beta d^3 \mathbf{r} d\tau e^{-i\mathbf{k} \cdot \mathbf{r} + i\omega_n \tau} \psi(\mathbf{r}, \tau) \\ \psi(\mathbf{r}, \tau) &= \frac{1}{\beta} \sum_n \int_\Omega \frac{d^3 \mathbf{k}}{(2\pi)^3} e^{i\mathbf{k} \cdot \mathbf{r} - i\omega_n \tau} \psi(\mathbf{k}, \omega_n). \end{aligned} \quad (\text{S11})$$

Suppose that the Hamiltonian of a non-interacting system is h_0 in the absence of disorder, and h_0 is time-independent and local, which can be denoted as $h_0 = h_0(\mathbf{r}, \nabla \mathbf{r}, \dots)$. The effective action in the presence of various types of disorders can be written as

$$\begin{aligned} S_{\text{eff}} = & \int d^3 \mathbf{r} d\tau \sum_{i=1}^N \bar{\psi}_i(\mathbf{r}, \tau) (\partial_\tau + h_0) \psi_i(\mathbf{r}, \tau) \\ & - \int d^3 \mathbf{r} d\tau d\tau' \sum_{i,j=1}^N \sum_{m=1}^M \frac{\Delta_m}{2} (\bar{\psi}_i A_m \psi_i)_{\mathbf{r}, \tau} (\bar{\psi}_j A_m \psi_j)_{\mathbf{r}, \tau'}. \end{aligned} \quad (\text{S12})$$

The Fourier transformed S_{eff} (imaginary time) reads

$$\begin{aligned}
S_{\text{eff}} &= \frac{1}{\beta} \sum_n \int \frac{d^3 \mathbf{k}}{(2\pi)^3} \sum_{i=1}^N \bar{\psi}_i(\mathbf{k}, \omega_n) [-i\omega_n + h_0(\mathbf{k})] \psi_i(\mathbf{k}, \omega_n) \\
&\quad - \frac{1}{\beta^2} \sum_{n, n'} \int \frac{d^3 \mathbf{k}_1}{(2\pi)^3} \frac{d^3 \mathbf{k}_2}{(2\pi)^3} \frac{d^3 \mathbf{k}_3}{(2\pi)^3} \frac{d^3 \mathbf{k}_4}{(2\pi)^3} (2\pi)^3 \delta(\mathbf{k}_1 + \mathbf{k}_3 - \mathbf{k}_2 - \mathbf{k}_4) \\
&\quad \times \sum_{i,j=1}^N \sum_{m=1}^M \frac{\Delta_m}{2} [\bar{\psi}_i(\mathbf{k}_1, \omega_n) A_m \psi_i(\mathbf{k}_2, \omega_n)] \cdot [\bar{\psi}_j(\mathbf{k}_3, \omega_{n'}) A_m \psi_j(\mathbf{k}_4, \omega_{n'})].
\end{aligned} \tag{S13}$$

In the following analyses of two-band models, all types of disorders are considered. The disorder potential is

$$U(\mathbf{r}) = U_0(\mathbf{r})\sigma_0 + U_x(\mathbf{r})\sigma_x + U_y(\mathbf{r})\sigma_y + U_z(\mathbf{r})\sigma_z. \tag{S14}$$

where the first term is the chemical-potential-type disorder and the last three terms are the magnetic-type disorders in the three directions [4]. The distribution is $p[U_m(\mathbf{r})] \propto \exp[-\frac{1}{2\Delta_m} d^3 \mathbf{r} U_m(\mathbf{r})^2]$ for $m = 0, x, y, z$. After performing the replica method, the effective action $S_{\text{eff}} = S_0 + S_1$ includes both the non-interacting part

$$S_0 = \int d^3 \mathbf{r} d\tau \sum_{i=1}^N \bar{\psi}_i(\mathbf{r}, \tau) [\partial_\tau + H(\mathbf{r}, \nabla \mathbf{r}, \dots) - \mu] \psi_i(\mathbf{r}, \tau) \tag{S15}$$

and the disorder induced effective interaction part

$$S_1 = - \int d^3 \mathbf{r} d\tau d\tau' \sum_{i,j=1}^N \sum_{m=0,x,y,z} \frac{\Delta_m}{2} (\bar{\psi}_i \sigma_m \psi_i)_{\mathbf{r},\tau} (\bar{\psi}_j \sigma_m \psi_j)_{\mathbf{r},\tau'}. \tag{S16}$$

III. RG STEP 1: COARSE GRAIN

We use the momentum-shell RG method [3, 5–10] to analyse the knot transitions of nodal-knot semimetals with Hamiltonian $H(\mathbf{k}) = f_x(\mathbf{k})\sigma_x + f_y(\mathbf{k})\sigma_y$ under the weak disorder regime. The disorder strengths Δ_m ($m = 0, x, y, z$) can be viewed as small parameters.

The fermionic field $\psi(\mathbf{k}, \omega_n)$ is decoupled into a “slow” mode $\psi_{<}(\mathbf{k}, \omega_n)$ and a “fast” mode $\psi_{>}(\mathbf{k}, \omega_n)$, which is defined as

$$\begin{aligned}
\psi_{<}(\mathbf{k}, \omega_n) &= \Theta\left(\frac{\Lambda}{b} - |k|\right) \psi(\mathbf{k}, \omega_n), \\
\psi_{>}(\mathbf{k}, \omega_n) &= \Theta(\Lambda - |k|) \Theta\left(|k| - \frac{\Lambda}{b}\right) \psi(\mathbf{k}, \omega_n).
\end{aligned} \tag{S17}$$

Here, Λ is the momentum cutoff. $b = e^l$ is the scaling factor with l the running scale parameter. The “fast” mode lies on the momentum-shell that is to be integrated out.

The effective action can be rewritten as:

$$\begin{aligned}
S_0 &= S_{0,<} + S_{0,>} \\
S_1 &= S_{1,<} + S_{1,>},
\end{aligned} \tag{S18}$$

where

$$\begin{aligned}
S_{0,<} &= \int d^3 \mathbf{r} d\tau \sum_{i=1}^N \bar{\psi}_{i,<}(\mathbf{r}, \tau) (\partial_\tau + H - \mu) \psi_{i,<}(\mathbf{r}, \tau) \\
&= \frac{1}{\beta} \sum_n \int \frac{d^3 \mathbf{k}}{(2\pi)^3} \sum_{i=1}^N \bar{\psi}_{i,<}(\mathbf{k}, \omega_n) [-i\omega_n + H(\mathbf{k}) - \mu] \psi_{i,<}(\mathbf{k}, \omega_n)
\end{aligned} \tag{S19}$$

$$\begin{aligned}
S_{0,>} &= \int d^3 \mathbf{r} d\tau \sum_{i=1}^N \bar{\psi}_{i,>}(\mathbf{r}, \tau) (\partial_\tau + H - \mu) \psi_{i,>}(\mathbf{r}, \tau) \\
&= \frac{1}{\beta} \sum_n \int \frac{d^3 \mathbf{k}}{(2\pi)^3} \sum_{i=1}^N \bar{\psi}_{i,>}(\mathbf{k}, \omega_n) [-i\omega_n + H(\mathbf{k}) - \mu] \psi_{i,>}(\mathbf{k}, \omega_n).
\end{aligned} \tag{S20}$$

$$\begin{aligned}
S_{1,<} = & -\frac{1}{\beta^2} \sum_{n,n'} \int \frac{d^3\mathbf{k}_1}{(2\pi)^3} \frac{d^3\mathbf{k}_2}{(2\pi)^3} \frac{d^3\mathbf{k}_3}{(2\pi)^3} \frac{d^3\mathbf{k}_4}{(2\pi)^3} (2\pi)^3 \delta(\mathbf{k}_1 + \mathbf{k}_3 - \mathbf{k}_2 - \mathbf{k}_4) \\
& \times \sum_{i,j=1}^N \sum_{m=0,x,y,z} \frac{\Delta_m}{2} [\bar{\psi}_{i,<}(\mathbf{k}_1, \omega_n) \sigma_m \psi_{i,<}(\mathbf{k}_2, \omega_n)] \cdot [\bar{\psi}_{j,<}(\mathbf{k}_3, \omega_{n'}) \sigma_m \psi_{j,<}(\mathbf{k}_4, \omega_{n'})]. \tag{S21}
\end{aligned}$$

and

$$\begin{aligned}
S_{1,>} = & -\frac{1}{\beta^2} \sum_{n,n'} \int \frac{d^3\mathbf{k}_1}{(2\pi)^3} \frac{d^3\mathbf{k}_2}{(2\pi)^3} \frac{d^3\mathbf{k}_3}{(2\pi)^3} \frac{d^3\mathbf{k}_4}{(2\pi)^3} (2\pi)^3 \delta(\mathbf{k}_1 + \mathbf{k}_3 - \mathbf{k}_2 - \mathbf{k}_4) \\
& \times \sum_{i,j=1}^N \sum_{m=0,x,y,z} \sum_{\substack{\text{at least one} \\ \alpha\beta\gamma\delta}} > \frac{\Delta_m}{2} [\bar{\psi}_{i,\alpha}(\mathbf{k}_1, \omega_n) \sigma_m \psi_{i,\beta}(\mathbf{k}_2, \omega_n)] \cdot [\bar{\psi}_{j,\gamma}(\mathbf{k}_3, \omega_{n'}) \sigma_m \psi_{j,\delta}(\mathbf{k}_4, \omega_{n'})]. \tag{S22}
\end{aligned}$$

The functional integral can be rewritten explicitly in terms of $>$ and $<$ as

$$\begin{aligned}
\langle \mathcal{Z}^N \rangle_{\text{dis}} = \mathcal{Z}_{\text{eff}} &= \int \mathcal{D}[\bar{\psi}_{<}, \psi_{<}; \bar{\psi}_{>}, \psi_{>}] e^{-S_{\text{eff}}} \\
&= \int \mathcal{D}[\bar{\psi}_{<}, \psi_{<}; \bar{\psi}_{>}, \psi_{>}] e^{-S_{0,<} - S_{0,>} - S_{1,<} - S_{1,>}} \\
&= \int \mathcal{D}[\bar{\psi}_{<}, \psi_{<}] e^{-S_{0,<} - S_{1,<}} \int \mathcal{D}[\bar{\psi}_{>}, \psi_{>}] e^{-S_{0,>} - S_{1,>}} \\
&= \mathcal{Z}_{0,>} \int \mathcal{D}[\bar{\psi}_{<}, \psi_{<}] e^{-S_{0,<} - S_{1,<}} \langle e^{-S_{1,>}} \rangle_{0,>} \\
&= \mathcal{Z}_{0,>} \int \mathcal{D}[\bar{\psi}_{<}, \psi_{<}] e^{-S_{0,<} - S_{1,<}} e^{-\langle S_{1,>} \rangle_{0,>} + \frac{1}{2} (\langle S_{1,>}^2 \rangle_{0,>} - \langle S_{1,>} \rangle_{0,>}^2) + \dots} \tag{S23}
\end{aligned}$$

where the average over the fast modes is defined as

$$\langle \dots \rangle_{0,>} = \frac{\int \mathcal{D}[\bar{\psi}_{>}, \psi_{>}] e^{-S_{0,>}} (\dots)}{\int \mathcal{D}[\bar{\psi}_{>}, \psi_{>}] e^{-S_{0,>}}} \tag{S24}$$

and $\mathcal{Z}_{0,>} = \int \mathcal{D}[\bar{\psi}_{>}, \psi_{>}] e^{-S_{0,>}}$.

To the first order in Δ_m , only one diagram should be considered as shown in Fig. S1. The modification of $S_{0,<}$ from $S_{1,>}$ is

$$\delta S_{0,<} = \langle S_{1,>} \rangle_{0,>}, \tag{S25}$$

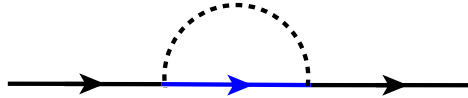


FIG. S1. Diagram for the first order perturbation. Black legs denote the “slow” modes and the blue legs denote the “fast” modes that should be integrated.

where

$$\begin{aligned}
\langle S_{1,>} \rangle_{0,>} &= -\frac{1}{\beta^2} \sum_{n,n'} \int \frac{d^3 \mathbf{k}_1}{(2\pi)^3} \frac{d^3 \mathbf{k}_2}{(2\pi)^3} \frac{d^3 \mathbf{k}_3}{(2\pi)^3} \frac{d^3 \mathbf{k}_4}{(2\pi)^3} (2\pi)^3 \delta(\mathbf{k}_1 + \mathbf{k}_3 - \mathbf{k}_2 - \mathbf{k}_4) \times \\
& 2 \sum_{i,j=1}^N \sum_{m=0,x,y,z} \frac{\Delta_m}{2} \bar{\psi}_{i,<}(\mathbf{k}_1, \omega_n) \sigma_m \langle \psi_{i,>}(\mathbf{k}_2, \omega_n) \bar{\psi}_{j,>}(\mathbf{k}_3, \omega_{n'}) \rangle_{0,>} \sigma_m \psi_{j,<}(\mathbf{k}_4, \omega_{n'}) \\
&= \frac{1}{\beta} \sum_n \int \frac{d^3 \mathbf{k}_1}{(2\pi)^3} \frac{d^3 \mathbf{k}_2}{(2\pi)^3} \sum_{i=1}^N \sum_{m=0,x,y,z} \Delta_m \bar{\psi}_{i,<}(\mathbf{k}_1, \omega_n) \sigma_m [G_0(\mathbf{k}_2, \omega_n)]_{(\mathbf{k}_2 \in >)} \sigma_m \psi_{i,<}(\mathbf{k}_1, \omega_n) \\
&= \frac{1}{\beta} \sum_n \int_{<} \frac{d^3 \mathbf{k}_1}{(2\pi)^3} \sum_{i=1}^N \sum_{m=0,x,y,z} \Delta_m \bar{\psi}_{i,<}(\mathbf{k}_1, \omega_n) \sigma_m \int_{>} \frac{d^3 \mathbf{k}_2}{(2\pi)^3} \frac{\mathbb{I}}{i\omega_n + \mu - f_x(\mathbf{k}_2)\sigma_x - f_y(\mathbf{k}_2)\sigma_y} \sigma_m \psi_{i,<}(\mathbf{k}_1, \omega_n).
\end{aligned} \tag{S26}$$

The integration of \mathbf{k}_2 is restricted on the momentum shell $\Lambda e^{-dl} < |\mathbf{k}_2| < \Lambda$. Thus the above equation becomes

$$\begin{aligned}
\delta S_{0,<} &= \frac{1}{\beta} \sum_n \int_{<} \frac{d^3 \mathbf{k}_1}{(2\pi)^3} \sum_{i=1}^N \sum_{m=0,x,y,z} \Delta_m \bar{\psi}_{i,<}(\mathbf{k}_1, \omega_n) \sigma_m \int \frac{\Lambda^3 d\mathbf{l} \sin\theta d\theta d\phi}{(2\pi)^3} \frac{\mathbb{I}}{i\omega_n + \mu - f_x\sigma_x - f_y\sigma_y} \sigma_m \psi_{i,<}(\mathbf{k}_1, \omega_n) \\
&= \frac{1}{\beta} \sum_n \int_{<} \frac{d^3 \mathbf{k}_1}{(2\pi)^3} \sum_{i=1}^N \sum_{m=0,x,y,z} \Delta_m \bar{\psi}_{i,<}(\mathbf{k}_1, \omega_n) \int \frac{\Lambda^3 d\mathbf{l} \sin\theta d\theta d\phi}{(2\pi)^3} \frac{-i\omega_n - \mu - f_x\sigma_m\sigma_x\sigma_m - f_y\sigma_m\sigma_y\sigma_m}{\omega_n^2 - \mu^2 - 2i\omega_n\mu + f_x^2 + f_y^2} \psi_{i,<}(\mathbf{k}_1, \omega_n).
\end{aligned} \tag{S27}$$

In the following, we consider the low frequency limit of the external leg, i.e., $\omega_n \rightarrow 0$. Define

$$\mathcal{G}_1^0 = \int \frac{\Lambda^3 \sin\theta d\theta d\phi}{(2\pi)^3} \frac{1}{f_x^2(\Lambda, \theta, \phi) + f_y^2(\Lambda, \theta, \phi) - \mu^2}, \tag{S28}$$

$$\mathcal{G}_1^x = \int \frac{\Lambda^3 \sin\theta d\theta d\phi}{(2\pi)^3} \frac{f_x(\Lambda, \theta, \phi)}{f_x^2(\Lambda, \theta, \phi) + f_y^2(\Lambda, \theta, \phi) - \mu^2}, \tag{S29}$$

$$\mathcal{G}_1^y = \int \frac{\Lambda^3 \sin\theta d\theta d\phi}{(2\pi)^3} \frac{f_y(\Lambda, \theta, \phi)}{f_x^2(\Lambda, \theta, \phi) + f_y^2(\Lambda, \theta, \phi) - \mu^2}, \tag{S30}$$

where $k_x = \Lambda \cos\phi \sin\theta$, $k_y = \Lambda \sin\phi \sin\theta$, and $k_z = \Lambda \cos\theta$. Then we have

$$\begin{aligned}
\delta S_{0,<} &= \frac{1}{\beta} \sum_n \int_{<} \frac{d^3 \mathbf{k}_1}{(2\pi)^3} \sum_{i=1}^N \bar{\psi}_{i,<}(\mathbf{k}_1, \omega_n) [(-i\omega_n - \mu)(\Delta_0 + \Delta_x + \Delta_y + \Delta_z) \mathcal{G}_1^0 dl \\
& + \sigma_x(-\Delta_0 - \Delta_x + \Delta_y + \Delta_z) \mathcal{G}_1^x dl + \sigma_y(-\Delta_0 + \Delta_x - \Delta_y + \Delta_z) \mathcal{G}_1^y dl] \psi_{i,<}(\mathbf{k}_1, \omega_n).
\end{aligned} \tag{S31}$$

To the second order in Δ_m , three types of diagrams should be considered as shown in Fig. S2. $S_{1,>}$ modifies $S_{1,<}$ as

$$\delta S_{1,<} = -\frac{1}{2} (\langle S_{1,>}^2 \rangle_{0,>} - \langle S_{1,>} \rangle_{0,>}^2). \tag{S32}$$

The contribution from Fig. S2 (a) is

$$\begin{aligned}
[\delta S_{1,<}]_{(a)} &= -\frac{1}{2} \times 2 \times 2 \times 2 \times \frac{1}{\beta^2} \sum_{n,n'} \int \frac{d^3 \mathbf{k}_1}{(2\pi)^3} \frac{d^3 \mathbf{k}_2}{(2\pi)^3} \frac{d^3 \mathbf{k}_3}{(2\pi)^3} \frac{d^3 \mathbf{k}_4}{(2\pi)^3} \frac{d^3 \mathbf{k}}{(2\pi)^3} (2\pi)^3 \delta(\mathbf{k}_1 + \mathbf{k}_3 - \mathbf{k}_2 - \mathbf{k}_4) \sum_{i,j=1}^N \sum_{m,m'=0,x,y,z} \frac{\Delta_m \Delta_{m'}}{4} \\
& \langle \bar{\psi}_{i,<}(\mathbf{k}_1, \omega_n) \sigma_m \psi_{i,<}(\mathbf{k}_2, \omega_n) \bar{\psi}_{j,>}(\mathbf{k} - \mathbf{q}, \omega_{n'}) \sigma_{m'} \psi_{j,>}(\mathbf{k}, \omega_{n'}) \bar{\psi}_{j,>}(\mathbf{k}, \omega_{n'}) \sigma_{m'} \psi_{j,<}(\mathbf{k}_4, \omega_{n'}) \bar{\psi}_{j,<}(\mathbf{k}_3, \omega_{n'}) \sigma_{m'} \psi_{j,>}(\mathbf{k} - \mathbf{q}, \omega_{n'}) \rangle_{0,>} \\
&= -\frac{1}{2} \times 2 \times 2 \times 2 \times \frac{1}{\beta^2} \sum_{n,n'} \int \frac{d^3 \mathbf{k}_1}{(2\pi)^3} \frac{d^3 \mathbf{k}_2}{(2\pi)^3} \frac{d^3 \mathbf{k}_3}{(2\pi)^3} \frac{d^3 \mathbf{k}_4}{(2\pi)^3} \frac{d^3 \mathbf{k}}{(2\pi)^3} (2\pi)^3 \delta(\mathbf{k}_1 + \mathbf{k}_3 - \mathbf{k}_2 - \mathbf{k}_4) \sum_{i,j=1}^N \sum_{m,m'=0,x,y,z} \frac{\Delta_m \Delta_{m'}}{4} \\
& \bar{\psi}_{i,<}(\mathbf{k}_1, \omega_n) \sigma_m \psi_{i,<}(\mathbf{k}_2, \omega_n) \bar{\psi}_{j,<}(\mathbf{k}_3, \omega_{n'}) \sigma_{m'} [G_0(\mathbf{k} - \mathbf{q}, \omega_{n'})] \sigma_m [G_0(\mathbf{k}, \omega_{n'})] \sigma_{m'} \psi_{j,<}(\mathbf{k}_4, \omega_{n'}),
\end{aligned} \tag{S33}$$

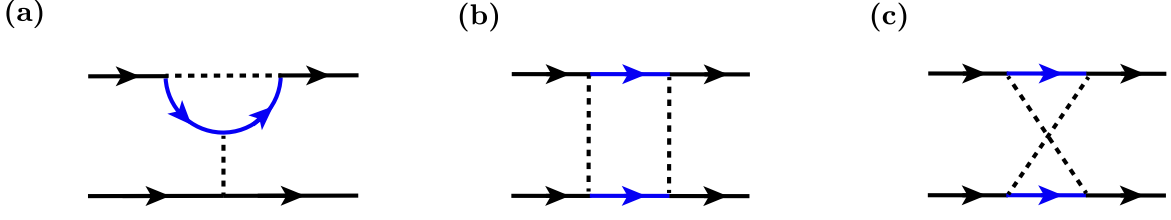


FIG. S2. Diagrams for the second order perturbation.

where $\mathbf{q} = \mathbf{k}_1 - \mathbf{k}_2$ is the transferred momentum. Note that the multiplications of 2's represent the symmetry factor of the Feynman diagrams. The contribution from Fig. S2 (b) is

$$\begin{aligned}
[\delta S_{1,<}]_{(b)} &= -\frac{1}{2} \times 2 \times 2 \times \frac{1}{\beta^2} \sum_{n,n'} \int \frac{d^3 \mathbf{k}_1}{(2\pi)^3} \frac{d^3 \mathbf{k}_2}{(2\pi)^3} \frac{d^3 \mathbf{k}_3}{(2\pi)^3} \frac{d^3 \mathbf{k}_4}{(2\pi)^3} \frac{d^3 \mathbf{k}}{(2\pi)^3} (2\pi)^3 \delta(\mathbf{k}_1 + \mathbf{k}_3 - \mathbf{k}_2 - \mathbf{k}_4) \sum_{i,j=1}^N \sum_{m,m'=0,x,y,z} \frac{\Delta_m \Delta_{m'}}{4} \\
&\langle \bar{\psi}_{i,<}(\mathbf{k}_1, \omega_n) \sigma_m \psi_{i,>}(\mathbf{k}, \omega_n) \bar{\psi}_{j,<}(\mathbf{k}_3, \omega_{n'}) \sigma_m \psi_{j,>}(\mathbf{q} - \mathbf{k}, \omega_{n'}) \bar{\psi}_{i,>}(\mathbf{k}, \omega_n) \sigma_{m'} \psi_{i,<}(\mathbf{k}_2, \omega_n) \bar{\psi}_{j,>}(\mathbf{q} - \mathbf{k}, \omega_{n'}) \sigma_{m'} \psi_{j,<}(\mathbf{k}_4, \omega_{n'}) \rangle_{0,>} \\
&= -\frac{1}{2} \times 2 \times 2 \times \frac{1}{\beta^2} \sum_{n,n'} \int \frac{d^3 \mathbf{k}_1}{(2\pi)^3} \frac{d^3 \mathbf{k}_2}{(2\pi)^3} \frac{d^3 \mathbf{k}_3}{(2\pi)^3} \frac{d^3 \mathbf{k}_4}{(2\pi)^3} \frac{d^3 \mathbf{k}}{(2\pi)^3} (2\pi)^3 \delta(\mathbf{k}_1 + \mathbf{k}_3 - \mathbf{k}_2 - \mathbf{k}_4) \sum_{i,j=1}^N \sum_{m,m'=0,x,y,z} \frac{\Delta_m \Delta_{m'}}{4} \\
&\bar{\psi}_{i,<}(\mathbf{k}_1, \omega_n) \sigma_m [G_0(\mathbf{k}, \omega_n)] \sigma_{m'} \psi_{i,<}(\mathbf{k}_2, \omega_n) \bar{\psi}_{j,<}(\mathbf{k}_3, \omega_{n'}) \sigma_m [G_0(\mathbf{q} - \mathbf{k}, \omega_{n'})] \sigma_{m'} \psi_{j,<}(\mathbf{k}_4, \omega_{n'}), \tag{S34}
\end{aligned}$$

where $\mathbf{q} = \mathbf{k}_1 + \mathbf{k}_3 = \mathbf{k}_2 + \mathbf{k}_4$.

The contribution from Fig. S2 (c) is

$$\begin{aligned}
[\delta S_{1,<}]_{(c)} &= -\frac{1}{2} \times 2 \times 2 \times \frac{1}{\beta^2} \sum_{n,n'} \int \frac{d^3 \mathbf{k}_1}{(2\pi)^3} \frac{d^3 \mathbf{k}_2}{(2\pi)^3} \frac{d^3 \mathbf{k}_3}{(2\pi)^3} \frac{d^3 \mathbf{k}_4}{(2\pi)^3} \frac{d^3 \mathbf{k}}{(2\pi)^3} (2\pi)^3 \delta(\mathbf{k}_1 + \mathbf{k}_3 - \mathbf{k}_2 - \mathbf{k}_4) \sum_{i,j=1}^N \sum_{m,m'=0,x,y,z} \frac{\Delta_m \Delta_{m'}}{4} \\
&\langle \bar{\psi}_{i,<}(\mathbf{k}_1, \omega_n) \sigma_m \psi_{i,>}(\mathbf{k}, \omega_n) \bar{\psi}_{j,>}(\mathbf{k} - \mathbf{q}, \omega_{n'}) \sigma_m \psi_{j,<}(\mathbf{k}_4, \omega_{n'}) \bar{\psi}_{i,>}(\mathbf{k}, \omega_n) \sigma_{m'} \psi_{i,<}(\mathbf{k}_2, \omega_n) \bar{\psi}_{j,<}(\mathbf{k}_3, \omega_{n'}) \sigma_{m'} \psi_{j,>}(\mathbf{k} - \mathbf{q}, \omega_{n'}) \rangle_{0,>} \\
&= -\frac{1}{2} \times 2 \times 2 \times \frac{1}{\beta^2} \sum_{n,n'} \int \frac{d^3 \mathbf{k}_1}{(2\pi)^3} \frac{d^3 \mathbf{k}_2}{(2\pi)^3} \frac{d^3 \mathbf{k}_3}{(2\pi)^3} \frac{d^3 \mathbf{k}_4}{(2\pi)^3} \frac{d^3 \mathbf{k}}{(2\pi)^3} (2\pi)^3 \delta(\mathbf{k}_1 + \mathbf{k}_3 - \mathbf{k}_2 - \mathbf{k}_4) \sum_{i,j=1}^N \sum_{m,m'=0,x,y,z} \frac{\Delta_m \Delta_{m'}}{4} \\
&\bar{\psi}_{i,<}(\mathbf{k}_1, \omega_n) \sigma_m [G_0(\mathbf{k}, \omega_n)] \sigma_{m'} \psi_{i,<}(\mathbf{k}_2, \omega_n) \bar{\psi}_{j,<}(\mathbf{k}_3, \omega_{n'}) \sigma_{m'} [G_0(\mathbf{k} - \mathbf{q}, \omega_{n'})] \sigma_m \psi_{j,<}(\mathbf{k}_4, \omega_{n'}), \tag{S35}
\end{aligned}$$

where $\mathbf{q} = \mathbf{k}_1 - \mathbf{k}_4$.

We take the \mathbf{q} 's in the above relations to be 0 for that we only consider external legs with small momentum, and $\omega_n = 0$ in the static limit. Moreover, the terms that emerge in $\delta S_{1,<}$ but do not appear in the original $S_{1,<}$ are omitted because they are of the order $O(\Delta^2)$ and break the constraint $\langle V_m(\mathbf{r}) V_n(\mathbf{r}') \rangle = \delta_{mn} \delta(\mathbf{r} - \mathbf{r}')$. Therefore, the modification of $S_{1,<}$ from the above diagrams can be summarized as

$$\begin{aligned}
\delta S_{1,<} = & -\frac{1}{\beta^2} \sum_{n,n'} \int \frac{d^3\mathbf{k}_1}{(2\pi)^3} \frac{d^3\mathbf{k}_2}{(2\pi)^3} \frac{d^3\mathbf{k}_3}{(2\pi)^3} \frac{d^3\mathbf{k}_4}{(2\pi)^3} (2\pi)^3 \delta(\mathbf{k}_1 + \mathbf{k}_3 - \mathbf{k}_2 - \mathbf{k}_4) \sum_{i,j=1}^N \frac{1}{2} \times \\
& \{ \bar{\psi}_{i,<}(\mathbf{k}_1, \omega_n) \sigma_0 \psi_{i,<}(\mathbf{k}_2, \omega_n) \bar{\psi}_{j,<}(\mathbf{k}_3, \omega_{n'}) \sigma_0 \psi_{j,<}(\mathbf{k}_4, \omega_{n'}) \\
& [2\Delta_0(\Delta_0 + \Delta_x + \Delta_y + \Delta_z)(\mu^2 \mathcal{G}_2^{00} + \mathcal{G}_2^{xx} + \mathcal{G}_2^{yy}) + 2(\Delta_0 \Delta_x - \Delta_y \Delta_z) \mathcal{G}_2^{x\bar{x}} + 2(\Delta_0 \Delta_y - \Delta_x \Delta_z) \mathcal{G}_2^{y\bar{y}} \\
& + \mu^2(\mathcal{G}_2^{00} + \mathcal{G}_2^{0\bar{0}})(\Delta_0^2 + \Delta_x^2 + \Delta_y^2 + \Delta_z^2) + 2(\Delta_0 \Delta_x + \Delta_y \Delta_z) \mathcal{G}_2^{xx} + 2(\Delta_0 \Delta_y + \Delta_x \Delta_z) \mathcal{G}_2^{yy}] dl \\
& + \bar{\psi}_{i,<}(\mathbf{k}_1, \omega_n) \sigma_x \psi_{i,<}(\mathbf{k}_2, \omega_n) \bar{\psi}_{j,<}(\mathbf{k}_3, \omega_{n'}) \sigma_x \psi_{j,<}(\mathbf{k}_4, \omega_{n'}) \\
& [2\Delta_x(\Delta_0 + \Delta_x - \Delta_y - \Delta_z)(\mu^2 \mathcal{G}_2^{00} + \mathcal{G}_2^{xx} - \mathcal{G}_2^{yy}) + (\Delta_0^2 + \Delta_x^2 + \Delta_y^2 + \Delta_z^2) \mathcal{G}_2^{x\bar{x}} + 2(\Delta_x \Delta_y - \Delta_0 \Delta_z) \mathcal{G}_2^{y\bar{y}} \\
& + 2(\Delta_0 \Delta_x - \Delta_y \Delta_z) \mu^2 \mathcal{G}_2^{0\bar{0}} + 2(\Delta_0 \Delta_x + \Delta_y \Delta_z) \mu^2 \mathcal{G}_2^{00} + (\Delta_0^2 + \Delta_x^2 + \Delta_y^2 + \Delta_z^2) \mathcal{G}_2^{xx} + 2(\Delta_0 \Delta_z + \Delta_x \Delta_y) \mathcal{G}_2^{yy} \\
& + 4\Delta_x(\Delta_0 + \Delta_x + \Delta_y + \Delta_z) \mu \mathcal{G}_2^{0x}] dl \\
& + \bar{\psi}_{i,<}(\mathbf{k}_1, \omega_n) \sigma_y \psi_{i,<}(\mathbf{k}_2, \omega_n) \bar{\psi}_{j,<}(\mathbf{k}_3, \omega_{n'}) \sigma_y \psi_{j,<}(\mathbf{k}_4, \omega_{n'}) \\
& [2\Delta_y(\Delta_0 + \Delta_y - \Delta_x - \Delta_z)(\mu^2 \mathcal{G}_2^{00} + \mathcal{G}_2^{yy} - \mathcal{G}_2^{xx}) + (\Delta_0^2 + \Delta_x^2 + \Delta_y^2 + \Delta_z^2) \mathcal{G}_2^{y\bar{y}} + 2(\Delta_x \Delta_y - \Delta_0 \Delta_z) \mathcal{G}_2^{x\bar{x}} \\
& + 2(\Delta_0 \Delta_y - \Delta_x \Delta_z) \mu^2 \mathcal{G}_2^{0\bar{0}} + 2(\Delta_0 \Delta_y + \Delta_x \Delta_z) \mu^2 \mathcal{G}_2^{00} + (\Delta_0^2 + \Delta_x^2 + \Delta_y^2 + \Delta_z^2) \mathcal{G}_2^{yy} + 2(\Delta_0 \Delta_z + \Delta_x \Delta_y) \mathcal{G}_2^{xx} \\
& + 4\Delta_y(\Delta_0 + \Delta_x + \Delta_y + \Delta_z) \mu \mathcal{G}_2^{0y}] dl \\
& + \bar{\psi}_{i,<}(\mathbf{k}_1, \omega_n) \sigma_z \psi_{i,<}(\mathbf{k}_2, \omega_n) \bar{\psi}_{j,<}(\mathbf{k}_3, \omega_{n'}) \sigma_z \psi_{j,<}(\mathbf{k}_4, \omega_{n'}) \\
& [2\Delta_z(-\Delta_0 + \Delta_x + \Delta_y - \Delta_z)(-\mu^2 \mathcal{G}_2^{00} + \mathcal{G}_2^{xx} + \mathcal{G}_2^{yy}) + 2(\Delta_x \Delta_z - \Delta_0 \Delta_y) \mathcal{G}_2^{x\bar{x}} + 2(\Delta_y \Delta_z - \Delta_0 \Delta_x) \mathcal{G}_2^{y\bar{y}} \\
& + 2(\Delta_0 \Delta_z - \Delta_x \Delta_y) \mu^2 \mathcal{G}_2^{0\bar{0}} + 2(\Delta_0 \Delta_z + \Delta_x \Delta_y) \mu^2 \mathcal{G}_2^{00} + 2(\Delta_0 \Delta_y + \Delta_x \Delta_z) \mathcal{G}_2^{xx} + 2(\Delta_0 \Delta_x + \Delta_y \Delta_z) \mathcal{G}_2^{yy}] dl \}. \tag{S36}
\end{aligned}$$

Here

$$\mathcal{G}_2^{00} = \int \frac{\Lambda^3 \sin\theta d\theta d\phi}{(2\pi)^3} \frac{1}{[f_x^2(\Lambda, \theta, \phi) + f_y^2(\Lambda, \theta, \phi) - \mu^2]^2}, \tag{S37}$$

$$\mathcal{G}_2^{0x} = \int \frac{\Lambda^3 \sin\theta d\theta d\phi}{(2\pi)^3} \frac{f_x(\Lambda, \theta, \phi)}{[f_x^2(\Lambda, \theta, \phi) + f_y^2(\Lambda, \theta, \phi) - \mu^2]^2}, \tag{S38}$$

$$\mathcal{G}_2^{0y} = \int \frac{\Lambda^3 \sin\theta d\theta d\phi}{(2\pi)^3} \frac{f_y(\Lambda, \theta, \phi)}{[f_x^2(\Lambda, \theta, \phi) + f_y^2(\Lambda, \theta, \phi) - \mu^2]^2}, \tag{S39}$$

$$\mathcal{G}_2^{xx} = \int \frac{\Lambda^3 \sin\theta d\theta d\phi}{(2\pi)^3} \frac{f_x^2(\Lambda, \theta, \phi)}{[f_x^2(\Lambda, \theta, \phi) + f_y^2(\Lambda, \theta, \phi) - \mu^2]^2}, \tag{S40}$$

$$\mathcal{G}_2^{yy} = \int \frac{\Lambda^3 \sin\theta d\theta d\phi}{(2\pi)^3} \frac{f_y^2(\Lambda, \theta, \phi)}{[f_x^2(\Lambda, \theta, \phi) + f_y^2(\Lambda, \theta, \phi) - \mu^2]^2}, \tag{S41}$$

$$\mathcal{G}_2^{0\bar{0}} = \int \frac{\Lambda^3 \sin\theta d\theta d\phi}{(2\pi)^3} \frac{1}{[f_x^2(\Lambda, \theta, \phi) + f_y^2(\Lambda, \theta, \phi) - \mu^2] \cdot [f_x^2(\Lambda, \pi - \theta, \pi + \phi) + f_y^2(\Lambda, \pi - \theta, \pi + \phi) - \mu^2]}, \tag{S42}$$

$$\mathcal{G}_2^{x\bar{x}} = \int \frac{\Lambda^3 \sin\theta d\theta d\phi}{(2\pi)^3} \frac{f_x(\Lambda, \theta, \phi) f_x(\Lambda, \pi - \theta, \pi + \phi)}{[f_x^2(\Lambda, \theta, \phi) + f_y^2(\Lambda, \theta, \phi) - \mu^2] \cdot [f_x^2(\Lambda, \pi - \theta, \pi + \phi) + f_y^2(\Lambda, \pi - \theta, \pi + \phi) - \mu^2]}, \tag{S43}$$

$$\mathcal{G}_2^{y\bar{y}} = \int \frac{\Lambda^3 \sin\theta d\theta d\phi}{(2\pi)^3} \frac{f_y(\Lambda, \theta, \phi) f_y(\Lambda, \pi - \theta, \pi + \phi)}{[f_x^2(\Lambda, \theta, \phi) + f_y^2(\Lambda, \theta, \phi) - \mu^2] \cdot [f_x^2(\Lambda, \pi - \theta, \pi + \phi) + f_y^2(\Lambda, \pi - \theta, \pi + \phi) - \mu^2]}. \tag{S44}$$

IV. RG STEP 2: RESCALE

After collecting all one-loop corrections, we perform the rescaling of space-time coordinates as

$$\begin{aligned}
\mathbf{r} &\rightarrow \mathbf{r}' = e^{-dl} \mathbf{r}, \\
\mathbf{k} &\rightarrow \mathbf{k}' = e^{dl} \mathbf{k}, \\
\tau &\rightarrow \tau' = e^{-\kappa dl} \tau, \\
\omega &\rightarrow \omega' = e^{\kappa dl} \omega.
\end{aligned} \tag{S45}$$

Then we introduce the renormalization constants

$$\psi = Z_\psi^{-1/2} \psi', \quad v_{p/q} = Z_{v_{p/q}}^{-1} v'_{p/q}, \quad \mu = Z_\mu^{-1} \mu', \quad \lambda_i = Z_{\lambda_i}^{-1} \lambda'_i, \quad m_i = Z_{m_i}^{-1} m'_i, \quad \Delta_i = Z_{\Delta_i}^{-1} \Delta'_i. \tag{S46}$$

The action in terms of the new variables reads (from now on we relabel X' 's to X 's for simplicity).

$$\begin{aligned}
S = & \int \frac{d^3 \mathbf{k}}{(2\pi)^3} \frac{d\omega}{2\pi} e^{-(3+\kappa)dl} \sum_{i=1}^N \frac{1}{Z_\psi} \bar{\psi}_i(\mathbf{k}, \omega) \{ -i\omega e^{-\kappa dl} [1 + (\Delta_0 + \Delta_x + \Delta_y + \Delta_z) \mathcal{G}_1^0 dl] - \frac{\mu}{Z_\mu} [1 + (\Delta_0 + \Delta_x + \Delta_y + \Delta_z) \mathcal{G}_1^0 dl] \\
& + [\frac{v_p}{Z_{v_p}} e^{-pdl} \text{Re}(k_x + ik_y)^p + \frac{v_q}{Z_{v_q}} \text{Re}(e^{-dl} k_z + i(\frac{\lambda_1}{Z_{\lambda_1}} - e^{-2dl} \frac{\lambda_2}{Z_{\lambda_2}} k^2))^q + \frac{m_1}{Z_{m_1}} + (-\Delta_0 - \Delta_x + \Delta_y + \Delta_z) \mathcal{G}_1^x dl] \sigma_x \\
& + [\frac{v_p}{Z_{v_p}} e^{-pdl} \text{Im}(k_x + ik_y)^p + \frac{v_q}{Z_{v_q}} \text{Im}(e^{-dl} k_z + i(\frac{\lambda_1}{Z_{\lambda_1}} - e^{-2dl} \frac{\lambda_2}{Z_{\lambda_2}} k^2))^q + \frac{m_2}{Z_{m_2}} + (-\Delta_0 + \Delta_x - \Delta_y + \Delta_z) \mathcal{G}_1^y dl] \sigma_y \} \psi_i(\mathbf{k}, \omega) \\
& - \frac{1}{2} \int \frac{d^3 \mathbf{k}_1}{(2\pi)^3} \frac{d^3 \mathbf{k}_2}{(2\pi)^3} \frac{d^3 \mathbf{k}_3}{(2\pi)^3} \frac{d^3 \mathbf{k}_4}{(2\pi)^3} (2\pi)^3 \delta(\mathbf{k}_1 + \mathbf{k}_3 - \mathbf{k}_2 - \mathbf{k}_4) \frac{d\omega'}{2\pi} \frac{d\omega}{2\pi} e^{-(2\kappa+9)dl} \times \\
& \sum_{i,j=1}^N \{ \frac{\Delta_0}{Z_\psi^2 Z_{\Delta_0}} \bar{\psi}_i(\mathbf{k}_1, \omega) \sigma_0 \psi_i(\mathbf{k}_2, \omega) \bar{\psi}_j(\mathbf{k}_3, \omega') \sigma_0 \psi_j(\mathbf{k}_4, \omega') \\
& [1 + [2(\Delta_0 + \Delta_x + \Delta_y + \Delta_z)(\mu^2 \mathcal{G}_2^{00} + \mathcal{G}_2^{xx} + \mathcal{G}_2^{yy}) + 2(\Delta_x \Delta_0 - \Delta_y \Delta_z) / \Delta_0 \mathcal{G}_2^{x\bar{x}} + 2(\Delta_y \Delta_0 - \Delta_x \Delta_z) / \Delta_0 \mathcal{G}_2^{y\bar{y}} \\
& + \mu^2 (\mathcal{G}_2^{00} + \mathcal{G}_2^{0\bar{0}}) (\Delta_0^2 + \Delta_x^2 + \Delta_y^2 + \Delta_z^2) / \Delta_0 + 2(\Delta_x \Delta_0 + \Delta_y \Delta_z) / \Delta_0 \mathcal{G}_2^{xx} + 2(\Delta_y \Delta_0 + \Delta_x \Delta_z) / \Delta_0 \mathcal{G}_2^{yy}] dl \\
& + \frac{\Delta_x}{Z_\psi^2 Z_{\Delta_x}} \bar{\psi}_i(\mathbf{k}_1, \omega) \sigma_x \psi_i(\mathbf{k}_2, \omega) \bar{\psi}_j(\mathbf{k}_3, \omega') \sigma_x \psi_j(\mathbf{k}_4, \omega') \\
& [1 + [2(\Delta_0 + \Delta_x - \Delta_y - \Delta_z)(\mu^2 \mathcal{G}_2^{00} + \mathcal{G}_2^{xx} - \mathcal{G}_2^{yy}) + (\Delta_0^2 + \Delta_x^2 + \Delta_y^2 + \Delta_z^2) / \Delta_x \mathcal{G}_2^{x\bar{x}} + 2(\Delta_x \Delta_y - \Delta_0 \Delta_z) / \Delta_x \mathcal{G}_2^{y\bar{y}} \\
& + 2(\Delta_0 \Delta_x - \Delta_y \Delta_z) / \Delta_x \mu^2 \mathcal{G}_2^{0\bar{0}} + 2(\Delta_0 \Delta_x + \Delta_y \Delta_z) / \Delta_x \mu^2 \mathcal{G}_2^{00} + 4(\Delta_0 + \Delta_x + \Delta_y + \Delta_z) \mu \mathcal{G}_2^{0x} \\
& + (\Delta_0^2 + \Delta_x^2 + \Delta_y^2 + \Delta_z^2) / \Delta_x \mathcal{G}_2^{xx} + 2(\Delta_0 \Delta_z + \Delta_x \Delta_y) / \Delta_x \mathcal{G}_2^{yy}] dl \\
& + \frac{\Delta_y}{Z_\psi^2 Z_{\Delta_y}} \bar{\psi}_i(\mathbf{k}_1, \omega) \sigma_y \psi_i(\mathbf{k}_2, \omega) \bar{\psi}_j(\mathbf{k}_3, \omega') \sigma_y \psi_j(\mathbf{k}_4, \omega') \\
& [1 + [2(\Delta_0 + \Delta_y - \Delta_x - \Delta_z)(\mu^2 \mathcal{G}_2^{00} + \mathcal{G}_2^{yy} - \mathcal{G}_2^{xx}) + (\Delta_0^2 + \Delta_y^2 + \Delta_x^2 + \Delta_z^2) / \Delta_y \mathcal{G}_2^{y\bar{y}} + 2(\Delta_x \Delta_y - \Delta_0 \Delta_z) / \Delta_y \mathcal{G}_2^{x\bar{x}} \\
& + 2(\Delta_0 \Delta_y - \Delta_x \Delta_z) / \Delta_y \mu^2 \mathcal{G}_2^{0\bar{0}} + 2(\Delta_0 \Delta_y + \Delta_x \Delta_z) / \Delta_y \mu^2 \mathcal{G}_2^{00} + 4(\Delta_0 + \Delta_x + \Delta_y + \Delta_z) \mu \mathcal{G}_2^{0y} \\
& + (\Delta_0^2 + \Delta_x^2 + \Delta_y^2 + \Delta_z^2) / \Delta_y \mathcal{G}_2^{yy} + 2(\Delta_0 \Delta_z + \Delta_x \Delta_y) / \Delta_y \mathcal{G}_2^{xx}] dl \\
& + \frac{\Delta_z}{Z_\psi^2 Z_{\Delta_z}} \bar{\psi}_i(\mathbf{k}_1, \omega) \sigma_z \psi_i(\mathbf{k}_2, \omega) \bar{\psi}_j(\mathbf{k}_3, \omega') \sigma_z \psi_j(\mathbf{k}_4, \omega') \\
& [1 + [2(-\Delta_0 + \Delta_x + \Delta_y - \Delta_z)(-\mu^2 \mathcal{G}_2^{00} + \mathcal{G}_2^{xx} + \mathcal{G}_2^{yy}) + 2(\Delta_x \Delta_z - \Delta_0 \Delta_y) / \Delta_z \mathcal{G}_2^{x\bar{x}} + 2(\Delta_y \Delta_z - \Delta_0 \Delta_x) / \Delta_z \mathcal{G}_2^{y\bar{y}} \\
& + 2(\Delta_0 \Delta_z - \Delta_x \Delta_y) / \Delta_z \mu^2 \mathcal{G}_2^{0\bar{0}} + 2(\Delta_0 \Delta_z + \Delta_x \Delta_y) / \Delta_z \mu^2 \mathcal{G}_2^{00} \\
& + 2(\Delta_0 \Delta_y + \Delta_x \Delta_z) / \Delta_z \mathcal{G}_2^{xx} + 2(\Delta_0 \Delta_x + \Delta_y \Delta_z) / \Delta_z \mathcal{G}_2^{yy}] dl \}.
\end{aligned} \tag{S47}$$

V. RG STEP 3: RENORMALIZATION AND THE RG EQUATIONS

By requiring that S is of the same form of the non-renormalized case but with rescaled space, time, and parameters, we obtain the renormalization constants as

$$\begin{aligned}
Z_\psi &= 1 + [-3 - 2\kappa + (\Delta_0 + \Delta_x + \Delta_y + \Delta_z)\mathcal{G}_1^0]dl, & Z_\mu &= 1 + \kappa dl, \\
Z_{v_p} &= 1 + [\kappa - p - (\Delta_0 + \Delta_x + \Delta_y + \Delta_z)\mathcal{G}_1^0]dl, & Z_{v_q} &= 1 + [\kappa - q - (\Delta_0 + \Delta_x + \Delta_y + \Delta_z)\mathcal{G}_1^0]dl, \\
Z_{\lambda_1} &= 1 + dl, & Z_{\lambda_2} &= 1 - dl, \\
Z_{m_1} &= 1 + [\kappa - (\Delta_0 + \Delta_x + \Delta_y + \Delta_z)\mathcal{G}_1^0 + (-\Delta_0 - \Delta_x + \Delta_y + \Delta_z)\mathcal{G}_1^x/m_1]dl, \\
Z_{m_2} &= 1 + [\kappa - (\Delta_0 + \Delta_x + \Delta_y + \Delta_z)\mathcal{G}_1^0 + (-\Delta_0 + \Delta_x - \Delta_y + \Delta_z)\mathcal{G}_1^y/m_2]dl, \\
Z_{\Delta_0} &= 1 + [2\kappa - 3 - 2(\Delta_0 + \Delta_x + \Delta_y + \Delta_z)\mathcal{G}_1^0 + 2(\Delta_0 + \Delta_x + \Delta_y + \Delta_z)(\mu^2\mathcal{G}_2^{00} + \mathcal{G}_2^{xx} + \mathcal{G}_2^{yy}) \\
&\quad + 2(\Delta_x\Delta_0 - \Delta_y\Delta_z)/\Delta_0\mathcal{G}_2^{x\bar{x}} + 2(\Delta_y\Delta_0 - \Delta_x\Delta_z)/\Delta_0\mathcal{G}_2^{y\bar{y}} + \mu^2(\mathcal{G}_2^{00} + \mathcal{G}_2^{0\bar{0}})(\Delta_0^2 + \Delta_x^2 + \Delta_y^2 + \Delta_z^2)/\Delta_0 \\
&\quad + 2(\Delta_x\Delta_0 + \Delta_y\Delta_z)/\Delta_0\mathcal{G}_2^{xx} + 2(\Delta_y\Delta_0 + \Delta_x\Delta_z)/\Delta_0\mathcal{G}_2^{yy}]dl, \\
Z_{\Delta_x} &= 1 + [2\kappa - 3 - 2(\Delta_0 + \Delta_x + \Delta_y + \Delta_z)\mathcal{G}_1^0 + 2(\Delta_0 + \Delta_x - \Delta_y - \Delta_z)(\mu^2\mathcal{G}_2^{00} + \mathcal{G}_2^{xx} - \mathcal{G}_2^{yy}) + (\Delta_0^2 + \Delta_x^2 + \Delta_y^2 + \Delta_z^2)/\Delta_x\mathcal{G}_2^{x\bar{x}} \\
&\quad + 2(\Delta_x\Delta_y - \Delta_0\Delta_z)/\Delta_x\mathcal{G}_2^{y\bar{y}} + 2(\Delta_0\Delta_x - \Delta_y\Delta_z)/\Delta_x\mu^2\mathcal{G}_2^{0\bar{0}} + 2(\Delta_0\Delta_x + \Delta_y\Delta_z)/\Delta_x\mu^2\mathcal{G}_2^{00} + 4(\Delta_0 + \Delta_x + \Delta_y + \Delta_z)\mu\mathcal{G}_2^{0x} \\
&\quad + (\Delta_0^2 + \Delta_x^2 + \Delta_y^2 + \Delta_z^2)/\Delta_x\mathcal{G}_2^{xx} + 2(\Delta_0\Delta_z + \Delta_x\Delta_y)/\Delta_x\mathcal{G}_2^{yy}]dl, \\
Z_{\Delta_y} &= 1 + [2\kappa - 3 - 2(\Delta_0 + \Delta_x + \Delta_y + \Delta_z)\mathcal{G}_1^0 + 2(\Delta_0 + \Delta_y - \Delta_x - \Delta_z)(\mu^2\mathcal{G}_2^{00} + \mathcal{G}_2^{yy} - \mathcal{G}_2^{xx}) + (\Delta_0^2 + \Delta_y^2 + \Delta_x^2 + \Delta_z^2)/\Delta_y\mathcal{G}_2^{y\bar{y}} \\
&\quad + 2(\Delta_x\Delta_y - \Delta_0\Delta_z)/\Delta_y\mathcal{G}_2^{x\bar{x}} + 2(\Delta_0\Delta_y - \Delta_x\Delta_z)/\Delta_y\mu^2\mathcal{G}_2^{0\bar{0}} + 2(\Delta_0\Delta_y + \Delta_x\Delta_z)/\Delta_y\mu^2\mathcal{G}_2^{00} + 4(\Delta_0 + \Delta_x + \Delta_y + \Delta_z)\mu\mathcal{G}_2^{0y} \\
&\quad + (\Delta_0^2 + \Delta_x^2 + \Delta_y^2 + \Delta_z^2)/\Delta_y\mathcal{G}_2^{yy} + 2(\Delta_0\Delta_z + \Delta_x\Delta_y)/\Delta_y\mathcal{G}_2^{xx}]dl, \\
Z_{\Delta_z} &= 1 + [2\kappa - 3 - 2(\Delta_0 + \Delta_x + \Delta_y + \Delta_z)\mathcal{G}_1^0 + 2(\Delta_0 - \Delta_x - \Delta_y + \Delta_z)(\mu^2\mathcal{G}_2^{00} - \mathcal{G}_2^{xx} - \mathcal{G}_2^{yy}) + 2(\Delta_x\Delta_z - \Delta_0\Delta_y)/\Delta_z\mathcal{G}_2^{x\bar{x}} \\
&\quad + 2(\Delta_y\Delta_z - \Delta_0\Delta_x)/\Delta_z\mathcal{G}_2^{y\bar{y}} + 2(\Delta_0\Delta_z - \Delta_x\Delta_y)/\Delta_z\mu^2\mathcal{G}_2^{0\bar{0}} + 2(\Delta_0\Delta_z + \Delta_x\Delta_y)/\Delta_z\mu^2\mathcal{G}_2^{00} \\
&\quad + 2(\Delta_0\Delta_y + \Delta_x\Delta_z)/\Delta_z\mathcal{G}_2^{xx} + 2(\Delta_0\Delta_x + \Delta_y\Delta_z)/\Delta_z\mathcal{G}_2^{yy}]dl. \tag{S48}
\end{aligned}$$

The renormalization group equations for the parameters are obtained according to

$$\frac{d\ln X}{dl} = \frac{dZ_X}{dl} \Big|_{l \rightarrow 0}. \tag{S49}$$

Here, X is some parameter but not the field ψ . Then we have the RG equations

$$\begin{aligned}
\frac{d\mu}{dl} &= \kappa\mu, & \frac{dv_p}{dl} &= v_p[\kappa - p - (\Delta_0 + \Delta_x + \Delta_y + \Delta_z)\mathcal{G}_1^0], & \frac{dv_q}{dl} &= v_q[\kappa - q - (\Delta_0 + \Delta_x + \Delta_y + \Delta_z)\mathcal{G}_1^0], \\
\frac{d\lambda_1}{dl} &= \lambda_1, & \frac{d\lambda_2}{dl} &= -\lambda_2, \\
\frac{dm_1}{dl} &= m_1[\kappa - (\Delta_0 + \Delta_x + \Delta_y + \Delta_z)\mathcal{G}_1^0] + (-\Delta_0 - \Delta_x + \Delta_y + \Delta_z)\mathcal{G}_1^x, \\
\frac{dm_2}{dl} &= m_2[\kappa - (\Delta_0 + \Delta_x + \Delta_y + \Delta_z)\mathcal{G}_1^0] + (-\Delta_0 + \Delta_x - \Delta_y + \Delta_z)\mathcal{G}_1^y, \\
\frac{d\Delta_0}{dl} &= \Delta_0[2\kappa - 3 - 2(\Delta_0 + \Delta_x + \Delta_y + \Delta_z)\mathcal{G}_1^0] + 2\Delta_0(\Delta_0 + \Delta_x + \Delta_y + \Delta_z)(\mu^2\mathcal{G}_2^{00} + \mathcal{G}_2^{xx} + \mathcal{G}_2^{yy}) \\
&\quad + 2(\Delta_x\Delta_0 - \Delta_y\Delta_z)\mathcal{G}_2^{x\bar{x}} + 2(\Delta_y\Delta_0 - \Delta_x\Delta_z)\mathcal{G}_2^{y\bar{y}} + \mu^2(\mathcal{G}_2^{00} + \mathcal{G}_2^{0\bar{0}})(\Delta_0^2 + \Delta_x^2 + \Delta_y^2 + \Delta_z^2) \\
&\quad + 2(\Delta_x\Delta_0 + \Delta_y\Delta_z)\mathcal{G}_2^{xx} + 2(\Delta_y\Delta_0 + \Delta_x\Delta_z)\mathcal{G}_2^{yy}, \\
\frac{d\Delta_x}{dl} &= \Delta_x[2\kappa - 3 - 2(\Delta_0 + \Delta_x + \Delta_y + \Delta_z)\mathcal{G}_1^0 + 2(\Delta_0 + \Delta_x - \Delta_y - \Delta_z)(\mu^2\mathcal{G}_2^{00} + \mathcal{G}_2^{xx} - \mathcal{G}_2^{yy}) + 4(\Delta_0 + \Delta_x + \Delta_y + \Delta_z)\mu\mathcal{G}_2^{0x} \\
&\quad + (\Delta_0^2 + \Delta_x^2 + \Delta_y^2 + \Delta_z^2)\mathcal{G}_2^{x\bar{x}} + 2(\Delta_x\Delta_y - \Delta_0\Delta_z)\mathcal{G}_2^{y\bar{y}} + 2(\Delta_0\Delta_x - \Delta_y\Delta_z)\mu^2\mathcal{G}_2^{0\bar{0}} + 2(\Delta_0\Delta_x + \Delta_y\Delta_z)\mu^2\mathcal{G}_2^{00} \\
&\quad + (\Delta_0^2 + \Delta_x^2 + \Delta_y^2 + \Delta_z^2)\mathcal{G}_2^{xx} + 2(\Delta_0\Delta_z + \Delta_x\Delta_y)\mathcal{G}_2^{yy}], \\
\frac{d\Delta_y}{dl} &= \Delta_y[2\kappa - 3 - 2(\Delta_0 + \Delta_x + \Delta_y + \Delta_z)\mathcal{G}_1^0 + 2(\Delta_0 + \Delta_y - \Delta_x - \Delta_z)(\mu^2\mathcal{G}_2^{00} + \mathcal{G}_2^{yy} - \mathcal{G}_2^{xx}) + 4(\Delta_0 + \Delta_x + \Delta_y + \Delta_z)\mu\mathcal{G}_2^{0y} \\
&\quad + (\Delta_0^2 + \Delta_y^2 + \Delta_x^2 + \Delta_z^2)\mathcal{G}_2^{y\bar{y}} + 2(\Delta_x\Delta_y - \Delta_0\Delta_z)\mathcal{G}_2^{x\bar{x}} + 2(\Delta_0\Delta_y - \Delta_x\Delta_z)\mu^2\mathcal{G}_2^{0\bar{0}} + 2(\Delta_0\Delta_y + \Delta_x\Delta_z)\mu^2\mathcal{G}_2^{00} \\
&\quad + (\Delta_0^2 + \Delta_x^2 + \Delta_y^2 + \Delta_z^2)\mathcal{G}_2^{yy} + 2(\Delta_0\Delta_z + \Delta_x\Delta_y)\mathcal{G}_2^{xx}], \\
\frac{d\Delta_z}{dl} &= \Delta_z[2\kappa - 3 - 2(\Delta_0 + \Delta_x + \Delta_y + \Delta_z)\mathcal{G}_1^0 + 2(\Delta_0 - \Delta_x - \Delta_y + \Delta_z)(\mu^2\mathcal{G}_2^{00} - \mathcal{G}_2^{xx} - \mathcal{G}_2^{yy}) \\
&\quad + 2(\Delta_x\Delta_z - \Delta_0\Delta_y)\mathcal{G}_2^{x\bar{x}} + 2(\Delta_y\Delta_z - \Delta_0\Delta_x)\mathcal{G}_2^{y\bar{y}} + 2(\Delta_0\Delta_z - \Delta_x\Delta_y)\mu^2\mathcal{G}_2^{0\bar{0}} + 2(\Delta_0\Delta_z + \Delta_x\Delta_y)\mu^2\mathcal{G}_2^{00} \\
&\quad + 2(\Delta_0\Delta_y + \Delta_x\Delta_z)\mathcal{G}_2^{xx} + 2(\Delta_0\Delta_x + \Delta_y\Delta_z)\mathcal{G}_2^{yy}]. \tag{S50}
\end{aligned}$$

By requiring that the k -linear terms are scale-invariant, we obtain the dynamical exponent

$$\kappa = 1 + (\Delta_0 + \Delta_x + \Delta_y + \Delta_z)\mathcal{G}_1^0. \quad (\text{S51})$$

The RG equations then become

$$\begin{aligned} \frac{d\mu}{dl} &= \mu[1 + (\Delta_0 + \Delta_x + \Delta_y + \Delta_z)\mathcal{G}_1^0], & \frac{dv_p}{dl} &= (1-p)v_p, & \frac{dv_q}{dl} &= (1-q)v_q, & \frac{d\lambda_1}{dl} &= \lambda_1, & \frac{d\lambda_2}{dl} &= -\lambda_2, \\ \frac{dm_1}{dl} &= m_1 + (-\Delta_0 - \Delta_x + \Delta_y + \Delta_z)\mathcal{G}_1^x, & \frac{dm_2}{dl} &= m_2 + (-\Delta_0 + \Delta_x - \Delta_y + \Delta_z)\mathcal{G}_1^y, \\ \frac{d\Delta_0}{dl} &= -\Delta_0 + 2\Delta_0(\Delta_0 + \Delta_x + \Delta_y + \Delta_z)(\mu^2\mathcal{G}_2^{00} + \mathcal{G}_2^{xx} + \mathcal{G}_2^{yy}) \\ &\quad + 2(\Delta_x\Delta_0 - \Delta_y\Delta_z)\mathcal{G}_2^{x\bar{x}} + 2(\Delta_y\Delta_0 - \Delta_x\Delta_z)\mathcal{G}_2^{y\bar{y}} + \mu^2(\mathcal{G}_2^{00} + \mathcal{G}_2^{0\bar{0}})(\Delta_0^2 + \Delta_x^2 + \Delta_y^2 + \Delta_z^2) \\ &\quad + 2(\Delta_x\Delta_0 + \Delta_y\Delta_z)\mathcal{G}_2^{xx} + 2(\Delta_y\Delta_0 + \Delta_x\Delta_z)\mathcal{G}_2^{yy}, \\ \frac{d\Delta_x}{dl} &= -\Delta_x + 2\Delta_x(\Delta_0 + \Delta_x - \Delta_y - \Delta_z)(\mu^2\mathcal{G}_2^{00} + \mathcal{G}_2^{xx} - \mathcal{G}_2^{yy}) + 4\Delta_x(\Delta_0 + \Delta_x + \Delta_y + \Delta_z)\mu\mathcal{G}_2^{0x} \\ &\quad + (\Delta_0^2 + \Delta_x^2 + \Delta_y^2 + \Delta_z^2)\mathcal{G}_2^{x\bar{x}} + 2(\Delta_x\Delta_y - \Delta_0\Delta_z)\mathcal{G}_2^{y\bar{y}} + 2(\Delta_0\Delta_x - \Delta_y\Delta_z)\mu^2\mathcal{G}_2^{0\bar{0}} + 2(\Delta_0\Delta_x + \Delta_y\Delta_z)\mu^2\mathcal{G}_2^{00} \\ &\quad + (\Delta_0^2 + \Delta_x^2 + \Delta_y^2 + \Delta_z^2)\mathcal{G}_2^{xx} + 2(\Delta_0\Delta_z + \Delta_x\Delta_y)\mathcal{G}_2^{yy}, \\ \frac{d\Delta_y}{dl} &= -\Delta_y + 2\Delta_y(\Delta_0 - \Delta_x + \Delta_y - \Delta_z)(\mu^2\mathcal{G}_2^{00} + \mathcal{G}_2^{yy} - \mathcal{G}_2^{xx}) + 4\Delta_y(\Delta_0 + \Delta_x + \Delta_y + \Delta_z)\mu\mathcal{G}_2^{0y} \\ &\quad + (\Delta_0^2 + \Delta_y^2 + \Delta_x^2 + \Delta_z^2)\mathcal{G}_2^{y\bar{y}} + 2(\Delta_x\Delta_y - \Delta_0\Delta_z)\mathcal{G}_2^{x\bar{x}} + 2(\Delta_0\Delta_y - \Delta_x\Delta_z)\mu^2\mathcal{G}_2^{0\bar{0}} + 2(\Delta_0\Delta_y + \Delta_x\Delta_z)\mu^2\mathcal{G}_2^{00} \\ &\quad + (\Delta_0^2 + \Delta_x^2 + \Delta_y^2 + \Delta_z^2)\mathcal{G}_2^{yy} + 2(\Delta_0\Delta_z + \Delta_x\Delta_y)\mathcal{G}_2^{xx}, \\ \frac{d\Delta_z}{dl} &= -\Delta_z + 2\Delta_z(\Delta_0 - \Delta_x - \Delta_y + \Delta_z)(\mu^2\mathcal{G}_2^{00} - \mathcal{G}_2^{xx} - \mathcal{G}_2^{yy}) + 2(\Delta_x\Delta_z - \Delta_0\Delta_y)\mathcal{G}_2^{x\bar{x}} + 2(\Delta_y\Delta_z - \Delta_0\Delta_x)\mathcal{G}_2^{y\bar{y}} \\ &\quad + 2(\Delta_0\Delta_z - \Delta_x\Delta_y)\mu^2\mathcal{G}_2^{0\bar{0}} + 2(\Delta_0\Delta_z + \Delta_x\Delta_y)\mu^2\mathcal{G}_2^{00} + 2(\Delta_0\Delta_y + \Delta_x\Delta_z)\mathcal{G}_2^{xx} + 2(\Delta_0\Delta_x + \Delta_y\Delta_z)\mathcal{G}_2^{yy}. \end{aligned} \quad (\text{S52})$$

In the absence of disorder, the parameters depends on l in a simple manner as

$$\begin{aligned} \mu(l) &= \mu(l=0)e^l, & v_p(l) &= v_p(l=0)e^{(1-p)l}, & v_q(l) &= v_q(l=0)e^{(1-q)l}, \\ \lambda_1(l) &= \lambda_1(l=0)e^l, & \lambda_2(l) &= \lambda_2(l=0)e^{-l}, & m_i(l) &= m_i(l=0)e^l. \end{aligned} \quad (\text{S53})$$

Equations. (6-8) in the main text can be obtained by setting $\mu = 0$ for Eq. S52. Specially, Eq. (7) or (8) in the main text are obtained by setting $\Delta_x = \Delta_y = \Delta_z = 0$ or $\Delta_0 = \Delta_x = \Delta_y = 0$. In numerating Eq. (S29), (S30), (S40), and (S41), we set

$$\begin{aligned} f_x(\mathbf{k}) &= v_2[k_x^2 - k_y^2 + k_z^2 - (\lambda_1 - \lambda_2 k^2)^2] + m_1, \\ f_y(\mathbf{k}) &= v_2[k_x k_y + k_z(\lambda_1 - \lambda_2 k^2)] + m_2, \end{aligned} \quad (\text{S54})$$

for the Hopf linked nodal-knots, and

$$\begin{aligned} f_x(\mathbf{k}) &= v_3[k_x^3 - 3k_x k_y^2 + k_z^3 - 3k_z(\lambda_1 - \lambda_2 k^2)^2] + m_1, \\ f_y(\mathbf{k}) &= v_3[3k_x^2 k_y - k_y^3 + 3k_z^2(\lambda_1 - \lambda_2 k^2) - (\lambda_1 - \lambda_2 k^2)^3] + m_2, \end{aligned} \quad (\text{S55})$$

for the valknot nodal-knots.

VI. KNOT WILSON LOOP INTEGRALS

We utilize the knot Wilson loop integral to characterize specific knot configurations to compensate for the limitations of solely using DOS markers to mark knot transition boundaries [11, 12]. The the knot Wilson loop gives rise to the total Berry phase accumulated by electrons as they traverse along the knotted nodal line and return to their original position. In the following, we first introduce the computational algorithm for the knot Wilson loop integral. Next, we present the results obtained through numerical calculations for systems with various configurations. Subsequently, we demonstrate the phase diagram determined jointly by DOS markers and the knot Berry phase. Finally, we discuss potential experimentally observables corresponding to the knot Wilson loop.

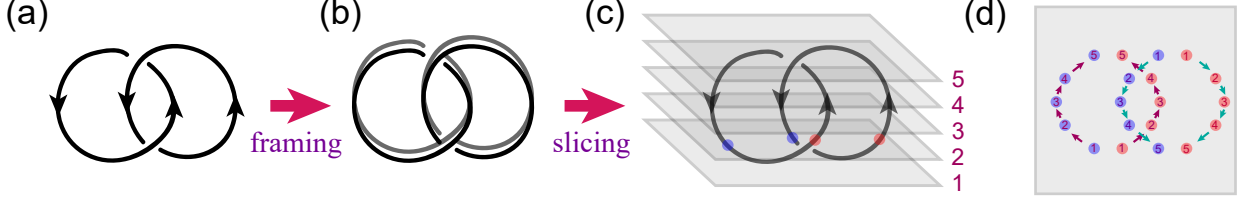


FIG. S3. Schematics of the numerical method to calculate the knot Wilson loop integral. (a), the Hopf-linked nodal-knot. (b), to avoid the singularity of the Berry phase on the nodal lines, the integral paths are slightly shifted from the nodal lines (the procedure was also called framing). (c), in calculating the Wilson loop integral, the 1D line integral in 3D Brillouin zone is sliced into many 2D layers (schematically numbered as 1-5). The directed integral paths intersects each layer at four points as shown by colored circles in (d). The colors (red or blue) of the circles denote the direction of the integral paths that pass the corresponding layer. The accumulated Berry phase can be obtained by counting the net phase changes of the intersection points (e.g. $\Delta\Phi = \Delta\Phi_{\text{red},1\rightarrow 5} - \Delta\Phi_{\text{blue},1\rightarrow 5}$).

We take the Hopf-linked nodal-knot as the example to calculate the knot Wilson loop. The knot Wilson loop with N oriented loops labeled by L_1, \dots, L_N (in the case of Hopf link, $N = 2$ and the two linked loops are labeled by L_1 and L_2) can be obtained through

$$W(L_1, \dots, L_N) = \frac{1}{\pi} \oint_{l \in L_1, \dots, L_N} \mathbf{A}(\mathbf{k}) \cdot d\mathbf{l}. \quad (\text{S56})$$

It yields the accumulated Berry phase along the Wilson loop, with $\mathbf{A}(\mathbf{k}) = -i\langle u_{\mathbf{k}} | \partial_{\mathbf{k}} | u_{\mathbf{k}} \rangle$ the Berry connection. Here,

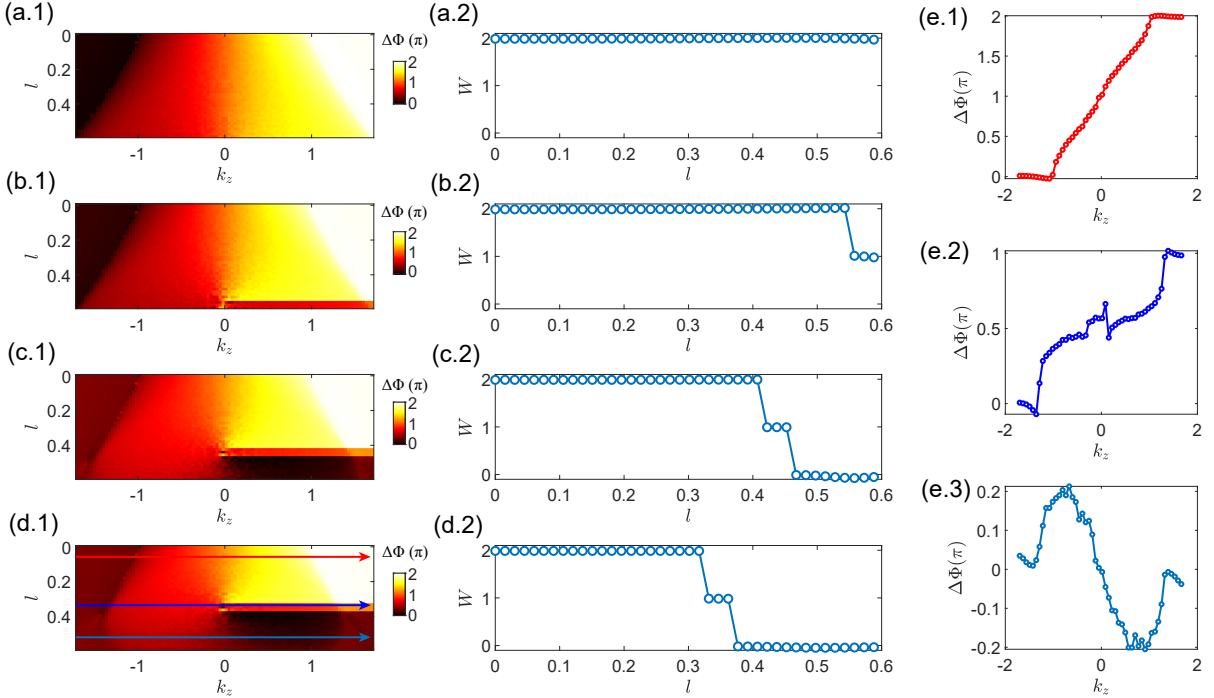


FIG. S4. Numerical results of the Wilson loop integral. The nodal-knot phase is the Hopf-linked phase with disorder type Δ_z , which is the same as Fig. 3 (c) and (d) in the main text, with $\Delta_z(0) = 0.12, 0.24, 0.36, 0.48$ from (a.1,2) to (d.1,2). The change of the accumulated Berry phase $\Delta\Phi$ with respect to k_z (which labels the slices as depicted in Fig. S3 (c)) from $k_z = -1.7$ to $k_z = 1.7$ and the renormalization scale l are shown in (a.1)-(d.1). The changes of Wilson loop integrals with respect to the renormalization scale l are shown in (a.2)-(d.2). Before the transition, the phase with $W = 2$ represents the Hopf-linked nodal-knot. After transition, $W = 0$ represents the unlinked phase. The variation of $\Delta\Phi$ with respect to k_z in (e.1)-(e.3) for three specific l as labeled in (d.1).

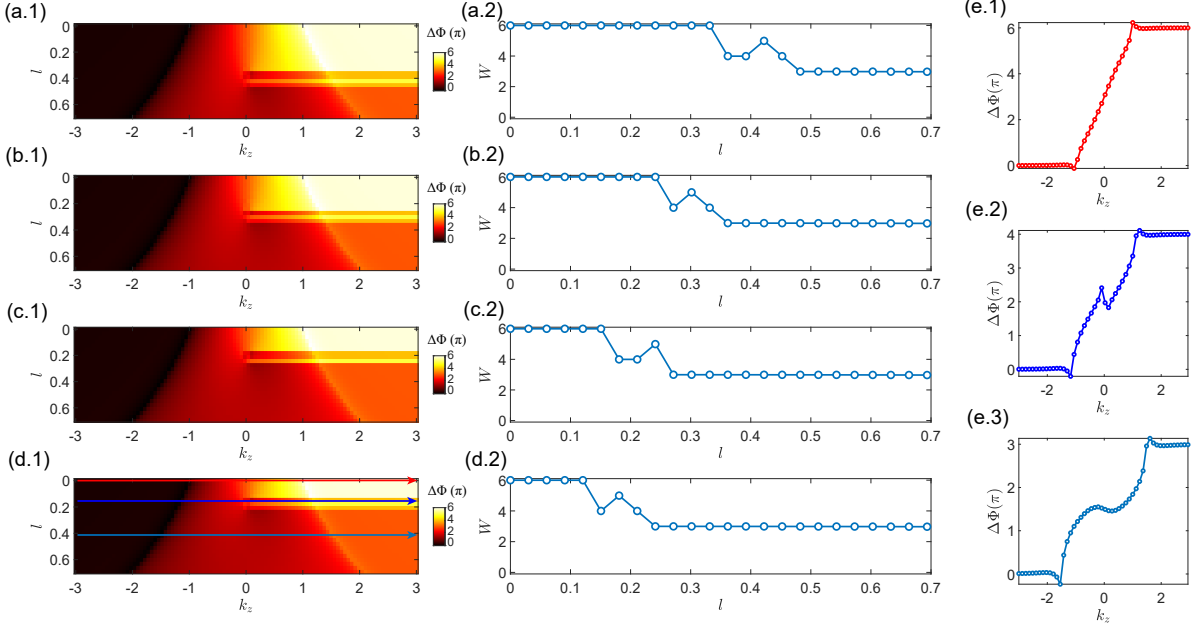


FIG. S5. Numerical results of the Wilson loop integral. The nodal-knot phase is the valknot phase with disorder type Δ_z , which is the same as Fig. 4 (c) and (d) in the main text, with $\Delta_z(0) = 0.3, 0.5, 0.7, 0.9$ from (a.1,2) to (d.1,2). The change of the accumulated Berry phase $\Delta\Phi$ with respect to k_z (which labels the slices as depicted in Fig. S3 (c)) from $k_z = -3$ to $k_z = 3$ and the renormalization scale l are shown in (a.1)-(d.1). The changes of Wilson loop integrals with respect to the renormalization scale l are shown in (a.2)-(d.2). Before the transition, the phase with $W = 6$ represents the valknot knot. After transition, $W = 3$ represents the trefoil knot phase. The variation of $\Delta\Phi$ with respect to k_z in (e.1)-(e.3) for three specific l as labeled in (d.1).

we consider the Wilson loop to be the nodal lines, and the orientation of the integral path \mathbf{l} is determined by the tangent vector $\mathbf{T}(\mathbf{k}_0)$ in Eq. (4) in the main text. We should also note that $\mathbf{A}(\mathbf{k})$ on the degenerate nodal lines are not well-defined, the Wilson loop integral should be slightly deviate from the nodal lines as depicted in Fig. S3 (b), and this procedure is sometimes called to “frame” the knots into strands (of which the idea was firstly proposed in Witten’s paper [11]). If a knot has non-trivial curls, i.e., non-zero writhe resulting from self-intersections in a particular projection direction, then naively framing in that direction can be problematic, meaning that the linking number between it and its frame might have extra contribution, thereby affecting the result for W . For structures like the Hopf link or unlink, we simply shift the z -coordinate of the nodal line by a small amount to serve as its frame [see Fig. S3 (a) and (b)], which, due to its simplicity, does not introduce new curls or writhe. For more complex situations, we can scale the nodal-knot configuration slightly in the radial (r) direction to obtain a frame configuration that ensures a single loop does not contribute to W .

To obtain the Berry phase along the Wilson loop, we slice 3D Brillouin zone into many 2D layers as schematically numbered as 1-5 in Fig. S3 (c). We view the directed Wilson loop as the worldline of quasi particles that intersect each layer at four points as shown by colored circles in (d), and the number in each circle denotes which layer the worldline intersects. Moreover, the colors (red or blue) of the circles denote the direction of the worldline that pass the corresponding layer. The Wilson loop integral can then be obtained by counting the net phase changes of the intersection points. Specifically, as demonstrated in Fig. S3 (d), as the slices go upward, the intersection points marked red (blue) between slice and the upward (downward) worldlines move in the slice plane. The upward going worldlines give the net positive Berry phase accumulation denoted by $\Delta\Phi_{\text{red}}$, and the downward going worldlines give the net negative Berry phase accumulation denoted by $\Delta\Phi_{\text{blue}}$. The total Berry phase along the worldline (thus the Wilson loop integral) is

$$\Delta\Phi = \Delta\Phi_{\text{red},1\rightarrow 5} - \Delta\Phi_{\text{blue},1\rightarrow 5} = \pi W(L_1, L_2). \quad (\text{S57})$$

Here, $1 \rightarrow 5$ means the five representative slices shown in S3 (c), and L_1 and L_2 denote the two loops that form the Hopf link.

In Fig. S4, we show the numerical results of the Wilson loop integral. The nodal-knot phase is the Hopf-linked phase with disorder type Δ_z , which is the same as Fig. 3 (c) and (d), with $\Delta_z(0) = 0.12, 0.24, 0.36, 0.48$ for Fig. S4

from (a.1,2) to (d.1,2). Specifically, the changes of Wilson loop integrals with respect to the renormalization scale l as shown in Fig. S4 (a.2)-(d.2) is reflected in the change of the accumulated Berry phase $\Delta\Phi$ (Eq. (S57)) with respect to k_z (which labels the slices as depicted in Fig. S3 (c)) from $k_z = -1.7$ to $k_z = 1.7$ shown in Fig. S4 (a.1)-(d.1). Clearly, as $\Delta_z(0)$ increases from 0.12 to 0.48, a transition in $\Delta\Phi$ arises as shown in Fig. S4 (c.1) and (d.1). Moreover, the corresponding $\Delta\Phi$ at $k_z = 1.7$, which is also the total Wilson loop integral $W = \pi\Delta\Phi$, is shown in Fig. S4 (a.2)-(d.2). Before the transition, the phase with $W = 2$ represents the Hopf-linked nodal-knot. After transition, $W = 0$ represents the unlinked phase. We also show the variation of $\Delta\Phi$ with respect to k_z in Fig. S4 (e.1)-(e.3) for three specific l as labeled Fig. S4 (d.1). From the plots we can clearly see that $\Delta\Phi$ increases from 0 to 2π for the Hopf link while go back to 0 for the unlink. Similarly, numerical results of the Wilson loop integral for the vorknot phase are shown in Fig. S5. The disorder type is Δ_z , which is the same as Fig. 4 (c) and (d) in the main text with $\Delta_z(0) = 0.3, 0.5, 0.7, 0.9$ from Fig. S5 (a.1,2) to (d.1,2). The change of the accumulated Berry phase $\Delta\Phi$ with respect to k_z from $k_z = -3$ to $k_z = 3$ and the renormalization scale l are shown in Fig. S5 (a.1)-(d.1). The changes of Wilson loop integrals with respect to the renormalization scale l are shown in Fig. S5 (a.2)-(d.2). Before the transition, the phase with $W = 6$ represents the vorknot knot. After transition, $W = 3$ represents the trefoil knot phase. The variation of $\Delta\Phi$ with respect to k_z in Fig. S5 (e.1)-(e.3) for three specific l as labeled in Fig. S5 (d.1).

By studying both the transitions in W and the singular behavior of the DOS marker near the knot transition points, the boundaries of the nodal-knot transitions can be determined more clearly. Moreover, the knot Wilson loop integral W indeed has real physical meaning and is not merely a mathematical quantity without observable effects. It can represent the total phase shifts for closed cyclotron orbits in the de Haas-van Alphen oscillation experiment.

VII. DISCUSSIONS ON DE HAAS-VAN ALPHEN EXPERIMENTS

Experimentally, determining the transition of the Fermi surface topologies (i.e., Lifshitz transition) is typically accomplished by combining transport measurements with quantum oscillation experiments. Therefore, we propose a potentially feasible way to reflect the nodal-knot structures and their transitions through de Haas-van Alphen oscillation experiment, as demonstrated in Fig. S6. Taking the Hopf link as an example, before the transition occurs, a magnetic field is applied perpendicular to one of the nodal loops. According to the semiclassical equations of motion [13]

$$\begin{aligned} \frac{d\mathbf{r}}{dt} &= \frac{\partial\epsilon(\mathbf{k})}{\hbar\partial\mathbf{k}} - \frac{d\mathbf{k}}{dt} \times \boldsymbol{\Omega}(\mathbf{k}), \\ \frac{\hbar d\mathbf{k}}{dt} &= -e\mathbf{E} - e\frac{d\mathbf{r}}{dt} \times \mathbf{B}, \end{aligned} \quad (\text{S58})$$

electrons undergo cyclotron motion in momentum space, moving perpendicular to the magnetic field and around the nodal loop, as indicated by the loops of different colors in the left panel. The area enclosed by its cyclotron orbit in momentum space is denoted by A_{orb} . When the magnetic field changes, the DOS exhibits periodic oscillations

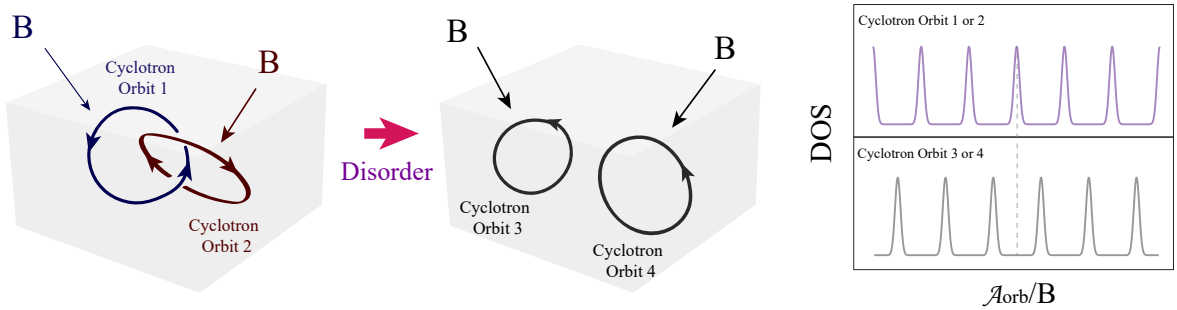


FIG. S6. A schematic diagram of utilizing the de Haas-van Alphen oscillation experiment to reflect the nodal-knot transition. Taking the Hopf link as an example, before the transition occurs, a magnetic field is applied perpendicular to one of the nodal loops. According to the semiclassical equations of motion, electrons undergo cyclotron motion in momentum space, moving perpendicular to the magnetic field and around the nodal loop, as indicated by the loops of different colors in the left panel. The area enclosed by its cyclotron orbit in momentum space is denoted by A_{orb} . When the magnetic field changes, the DOS exhibits periodic oscillations with A_{orb}/B , as shown in the right panel. Under the renormalization of disorder, the linked structure evolve to be unlinked, as shown in the middle panel. Applying a magnetic field in this situation still results in quantum oscillations, but the phase of the oscillation with A_{orb}/B shifts. This phase shift arises from the π Berry phase difference between the linked and unlinked structures.

with A_{orb}/B , as shown in the right panel. Under the renormalization of disorder, the linked structure evolve to be unlinked, as shown in the middle panel. Applying a magnetic field (it is worth noted that in this case the nodal loop may not lie this the same plane as before, thus the direction of \mathbf{B} needs to be adjusted. Moreover, the nodal loop itself may not be a planar curve, in order to form the cyclotron orbit, a finite chemical potential is needed) in this situation still results in quantum oscillations, but the phase of the oscillation with A_{orb}/B shifts. According to the Landau quantization rule

$$A_{\text{orb}}(\mathbf{k}_B) = 2\pi eB(n + 1/2 + \phi_B), \quad (\text{S59})$$

where $A_{\text{orb}}(\mathbf{k}_B)$ is the area of the cyclotron orbit with \mathbf{k}_B the wave vector along the \mathbf{B} direction, and ϕ_B is the Berry phase accumulated by the electrons during the cyclotron motion [14]. According to the Landau quantization rule, when two nodal loops are linked together, the cyclotron motion orbit of electrons on one nodal loop will encircle the other nodal loop. As we know, electrons encircling a nodal line will accumulate a Berry phase of π . Therefore, the Berry phase ϕ_B is π in this case. Under the renormalization of disorder, the linked nodal loops are separated, resulting in $\phi_B = 0$. The difference in the Berry phase ϕ_B thus induces the π Berry phase shift in the de Haas-van Alphen oscillation experiment as depicted in the right panel of Fig. S6. Therefore, these accumulated Berry phases ϕ_B for each nodal loop is unique for knotted nodal lines. If all the information of ϕ_B can be obtained, the nodal-knot structure can be determined to a large extent. Furthermore, we need to point out that this phase shift is closely related to the knot Wilson loop integral W . From the previous expressions, the knot Wilson loop integral precisely corresponds to the sum of the Berry phases ϕ_B accumulated by each cyclotron orbit.

-
- [1] F. Wegner, The Mobility Edge Problem: Continuous Symmetry and a Conjecture, *Z. Phys. B: Condens. Matter* **35**, 207 (1979).
- [2] P. A. Lee and T. V. Ramakrishnan, Disordered Electronic Systems, *Rev. Mod. Phys.* **57**, 287 (1985).
- [3] A. Altland and B. D. Simons, *Condensed Matter Field Theory*, 2nd ed. (Cambridge University Press, Cambridge, 2010).
- [4] A. W. W. Ludwig, M. P. A. Fisher, R. Shankar, and G. Grinstein, Integer Quantum Hall Transition: An Alternative Approach and Exact Results, *Phys. Rev. B* **50**, 7526 (1994).
- [5] J. Cardy, *Scaling and Renormalization in Statistical Physics*, Cambridge Lecture Notes in Physics (Cambridge University Press, Cambridge, 1996).
- [6] M. Kardar, *Statistical Physics of Fields* (Cambridge University Press, Cambridge, 2007).
- [7] P. Goswami and S. Chakravarty, Quantum Criticality Between Topological and Band Insulators in 3+1 Dimensions, *Phys. Rev. Lett.* **107**, 196803 (2011).
- [8] X. Luo, B. Xu, T. Ohtsuki, and R. Shindou, Quantum Multicriticality in Disordered Weyl Semimetals, *Phys. Rev. B* **97**, 045129 (2018).
- [9] P.-L. Zhao, H.-Z. Lu, and X.-C. Xie, Theory for Magnetic-Field-Driven 3D Metal-Insulator Transitions in the Quantum Limit, *Phys. Rev. Lett.* **127**, 046602 (2021).
- [10] H. Isobe and L. Fu, Supermetal, *Phys. Rev. Res.* **1**, 033206 (2019).
- [11] E. Witten, Quantum field theory and the Jones polynomial, *Commun.Math. Phys.* **121**, 351 (1989).
- [12] B. Lian, C. Vafa, F. Vafa, and S.-C. Zhang, Chern-Simons theory and Wilson loops in the Brillouin zone, *Phys. Rev. B* **95**, 094512 (2017).
- [13] D. Xiao, M.-C. Chang, and Q. Niu, Berry phase effects on electronic properties, *Rev. Mod. Phys.* **82**, 1959 (2010).
- [14] G. P. Mikitik and Y. V. Sharlai, Manifestation of Berry's Phase in Metal Physics, *Phys. Rev. Lett.* **82**, 2147 (1999).